Accepted to Phys. Fluids 10.1063/5.0123365

Detection of an internal solitary wave by the underwater vehicle based on machine learning

Miao Zhang (张淼), Haibao Hu (胡海豹), Peng Du (杜鹏)*, Xiaopeng Chen (陈效鹏), Zhuoyue Li (李卓越), Chao Wang (汪超), Lu Cheng (程路), Zijian Tang (唐子建)

(School of Marine Science and Technology, Northwestern Polytechnical University, Xi'an, 710072, China)

Email: dupeng@nwpu.edu.cn

Abstract

A new hydrodynamic artificial intelligence (AI) detection method is proposed to realize the accurate detection of internal solitary waves (ISWs) by the underwater vehicle. Two deep convolution neural network structures are established to predict the relative position between the underwater vehicle and ISW and the flow field around the underwater vehicle. By combining field observation data and the computational fluid dynamics (CFD) method, accurate numerical simulation of the motion of the underwater vehicle in a real ISW environment is achieved. The training process for the neural network is implemented by building a dataset from the above results. It is shown that the position prediction accuracy of the network for ISW is larger than 95%. For the prediction of the flow field around the underwater vehicle, it is found that the addition of the convolutional block attention module (CBAM) can increase the prediction accuracy. Moreover, the reduction of the number of sensors by the dynamic mode decomposition (DMD) method and k-means clustering method is realized. The accuracy can still reach 92% even when the number of sensors is reduced. This study is the first to use hydrodynamic signals for the detection of ISW, which can enhance the navigation safety of underwater vehicles.

Keywords

detection, artificial intelligence, internal solitary waves, deep convolutional neural network, underwater vehicle

1. Introduction

Internal solitary waves (ISWs) are active in marginal waters and widely distributed all over the world, such as in the northern South China Sea, the Sulu Sea, the Andaman Sea, the Washington Shelf, the North West Shelf of Australia, the Strait of Gibraltar, and the Massachusetts Bay [1]. These waves are mainly generated by stratified flows passing through rough terrains, such as ridges, submarine mountains, and canyons [2]. The large amplitude of ISWs can spread out over hundreds of kilometers and transport significant quantities of energy from the seabed to the sea surface [3][4]. This phenomenon transfers ocean nutrients from the top to the bottom, promoting biological growth. In addition, ISWs can generate strong shear, which poses a significant threat to the safety of marine

structures [5].

In recent years, researchers have made great progress in the theoretical analysis of ISWs. This can reveal the evolution pattern and physical mechanism of ISWs. At present, non-linear ISW theories, such as KdV (Korteweg-De Vries), mKdV (modified KdV), MCC (Miyata-Choi-Camassa), DJL (Dubreil-Jacotin-Long) [6], have been proposed. Based on the above theory, both numerical and experimental studies on the interaction between ISWs and underwater vehicles, offshore platforms and other structures emerged. Several typical marine structures have been studied in-depth. Since cylindrical structures are the basic components of many marine structures, it is of practical significance to study the hydrodynamics of cylindrical structures interacting with ISWs [7][8]. Adding the cylinders in tandem or side by side will affect the forces greatly, and the distance between the cylinders will have an effect as well. In addition, the diameter of the cylinder influences the propagation of ISWs at different wave amplitudes [9]. It is demonstrated that symmetrical vortex shedding behind the cylinder can modify the horizontal force. A further extension of the study to the underwater vehicle has more engineering implications. The force characteristics of a stationary underwater vehicle in an internal solitary wave can be investigated using numerical simulation [10] and experimental methods [11]. For the more general case, He et al. [12] investigated the hydrodynamic properties of an underwater vehicle travelling at a certain speed when encountering an internal solitary wave. These studies can provide strategies for the manipulation of underwater vehicles. In the case of more complex structures such as submerged floating tunnels [13] and floating platforms [14], the interaction between these structures and ISWs becomes more complicated. Forces and moments were measured, and a functional relationship was obtained between empirical coefficients, Reynolds number, and layer depth based on the experimental results. The dynamic response of the tube-joint-mooring coupled system was obtained using numerical simulations. The above studies reveal the mechanism and laws of marine structures encountering ISWs. However, it is a prerequisite to detect the coming of ISWs in advance to take actions. As a result, the detection of ISWs becomes crucial.

There are Several ISW detection methods. Remote sensing detection method is the most commonly used one [15]. The ISWs modulate the sea surface wave through the propagation of the shear flow field. This causes the convergence and divergence of waves on the ocean surface. Thus, the roughness of the ocean surface is changed, and the remote sensing image can detect the characteristic bright and dark stripes of ISWs [16]. The distribution [17], generation mechanism [18], propagation characteristics [19][20], and prediction of ISWs have been widely studied using remote sensing images. However, due to the complexity of the marine environment, it is difficult to predict the evolution of ISWs. Therefore, remote sensing is only limited to the early warning of the captured ISW. It is not able to predict the real-time position of ISWs for the underwater vehicles.

ISWs can also be predicted by field observations. Platforms, such as ships and moorings, are used to collect relevant signals by combining acoustic doppler current profilers (ADCP) and conductivity-temperature-depth (CTD) profilers. In the past several decades, the northern South China Sea has been a hot spot in marine ISW research. Studies have shown that the occurrence of ISW has a certain pattern, which is closely related to the tides. Lien et al. [21] used four sets of ADCP measurements in the South China Sea to measure nonlinear ISWs. The analysis showed that repeated sequences of large amplitude nonlinear ISWs occurred mainly in semidiurnal cycles with amplitudes modulated by a two-week tidal cycle. Alford et al. [22] detected 14 ISWs across Luzon Strait by arranging an array composed of 10 moorings. They found that waves appeared twice a day in a specific pattern, with larger and narrower "A" waves alternating with wider and smaller "B" waves. Ramp et al. [23] used four oceanographic moorings to observe the large amplitude ISWs near Luzon straight for one year. Through long-term observation, it was found that the observed waves were concentrated around the spring tide, and no waves were observed at the neap tide. A notable feature was the apparent lack of waves in winter. Besides, there was a correlation between the ISW generation and the terrain. Li et al. [24] studied the generation and evolution mechanism of ISWs using the time series observation data of nonlinear internal waves in the deep basin of the South China Sea. These observational studies have captured the mechanisms of ISW generation and propagation patterns in fixed areas. The occurrence of ISWs in the region can be effectively predicted by building a dataset [25]. However, due to the high cost of long-term observation and the limitation of the measurement area and time, this method is very difficult to provide real-time ISW warning for the underwater vehicles.

The above methods of remote sensing and field observation demonstrate deficiencies regarding the underwater real-time detection of the ISWs. Consequently, it is urgent to find a real-time and accurate detection method. Recently, with the rise of machine learning, the application of machine learning to hydrodynamic detection has been successful. The detection method arranges several sensors to sense the surrounding flow field. Then the artificial neural network is used to predict the object in front. Linear [26] and square arrays [27] composed of pressure or velocity sensors have been successfully applied to predict the shape of obstacles ahead. In addition, the 3D position of the object can be predicted by sensing the wake [28]. However, all of the above are directly using data from the flow field as input to the artificial neural network. It is not considered to carry the sensor array on the detection object. Liu et al. [29] arranged a ring of pressure sensors on an automatic underwater vehicle (AUV). The frequency of the object's motion was predicted using an artificial neural network by collecting information about the pressure fluctuations in the wake. In addition, Liu et al. [30] also predicted the angle of attack of AUVs by wake detection. However, unlike detecting parameters such as shape and position of the object using wake, the pitching motion of

the vehicle needs to be considered when detecting large scale ISW. In addition, the sensor layout as well as the sampling strategy also need to be considered.

This study proposes a new hydrodynamic detection method for the ISWs on underwater vehicles based on deep learning. The ISW flow field with different wave amplitudes is obtained by solving DJL equation. The calculated results are compared with the actual observation data to realize accurate flow field modeling. The free motion of the underwater vehicle interacting with ISWs is realized by coupling CFD and DJL theory. Sensors are placed on the surface of the underwater vehicle to realize the detection of ISWs. The data is transmitted to the deep neural network for training. The arrangement and number of the sensors are optimized using dynamic mode decomposition and k-means clustering. The predictions of the hydrodynamics and flow fields of the underwater vehicle are also realized.

2. Methodology

2.1 Formulation of the problem

The current work uses the standard SUBOFF model proposed by the defense advanced research projects agency (DARPA). To simplify the problem, the study adopts the bare hull (AFF-1) without appendages, with a scale of 5:1. The ISWs with wave amplitudes of 125m, 140m, 155m and 170m are obtained by solving the DJL equation. Their trough positions are (3000, -222.8), (3000, -242.9), (3000, -250.6) and (3000, -264.5), respectively. The characteristic wavelengths are 2041m, 1913m, 1842m and 1769m, respectively. The vehicle will be placed 500m to 1000m away from the wave trough in x-direction. In the y-direction, the distance is 50m to 250m. The final detection results are expressed in terms of the vehicle's relative position to the trough and the wave amplitude.

In the beginning, the number of pressure and wall shear stress sensors arranged for deep learning is 60 respectively. The arrangement of the sensors avoids the rears of the stern appendages and the sail, where strong vortex shedding tends to occur, which can increase the nonlinearity of the problem. These sensors record instantaneous signals of the flow field. Subsequently, SUBOFF is placed at different positions in the ISW and moves passively. The data measured by the sensors is transmitted to the deep learning model for training, to detect the ISW position and amplitude. The schematic of the detection process is shown in Fig. 1. The network structures (a) and (c) implement the detection of ISW and the prediction of the flow field around the underwater vehicle, respectively. Fig. 1(b) is the feature extraction part, shared by (a) and (c). The time series signals obtained from different position sensors are integrated into 60*60 image data by pre-processing. The former represents the number of samples over time and the latter represents the sensor position. Since the hydrodynamic signals include pressure and wall shear stress, the number of channels of the input format is 2. When adding (b) to the network of (a), neurons are connected through full connection,

and the relative position coordinates *x*, *y*, absolute length *r,* and amplitude are output for the detection of ISW. On the other hand, for (c), the signed distance function of the SUBOFF geometry is first downsampled to extract the spatial location information. After that, the output of (b) is inserted into the fully connected network and then upsampled. The final prediction of the flow field around SUBOFF is achieved. In summary, the information of the ISW and the flow field around the SUBOFF are obtained by the above methods.

2.2 Numerical method

2.2.1 Numerical generation of ISW

The main methods of ISW generation include gravity collapse mechanism, double push-pedal method, velocity inlet method, mass source method, and flow field initialization method. The study uses the initialization method, which involves solving the ISW theory. The continuous density stratification model follows the physical reality of the ocean and eliminates the inherent shortcomings of the discontinuous density model. The strong nonlinear DJL theory is applied to generate the ISWs. Under the conditions of non-rotating, incompressible, and Boussinesq approximation, the Navier Stokes equation can be expressed as follows:

$$\frac{\mathrm{D}u}{\mathrm{D}t} = -\frac{1}{\rho_0}\nabla p + \frac{\rho}{\rho_0}\mathbf{g} + \nu\nabla^2 u \tag{1}$$

$$\nabla \cdot u = 0 \tag{2}$$

$$\frac{\mathrm{D}\rho}{\mathrm{D}t} = \kappa\nabla^2\rho \tag{3}$$

where κ is the molecular diffusivity. ρ is expressed as $\rho = \rho_0 + \bar{\rho}(z) + \rho'(\mathbf{x},t)$. ρ_0 is the reference density, expressed as $(\rho_1 + \rho_2)/2$. $\rho'(\mathbf{x},t)$, accounts for the perturbations caused by the wave.

The processing assumes that the ocean bottom is flat and the fluid motion is two-dimensional, excluding interference from background flows. By transforming Euler's equations into one equation for isopycnal displacement, a permanent traveling wave solution can be obtained. Thus the fully non-linear DJL equation is formulated as follows:

$$\begin{aligned} &\nabla^2\eta + \frac{N^2(z-\eta)}{c^2}\eta = 0, \quad \eta = 0 \quad \text{at} \quad z = 0, -H \\ &\eta = 0 \quad \text{at} \quad |x| \to \infty \end{aligned} \tag{4}$$

where η is the isopycnal displacement. H is the water depth. c is the propagation speed. z is the vertical position of Cartesian coordinates. N is the definition of the buoyancy frequency.

$$N^2(z) = -\frac{g}{\rho_0}\frac{d\bar{\rho}(z)}{dz} \tag{5}$$

The vertical distribution of the background density is defined as a hyperbolic tangent boundary according to the description of the ISW solution by Deepwell et al [31].

$$\bar{\rho}(z,t=0)=\frac{\rho_1+\rho_2}{2}-\frac{\rho_2-\rho_1}{2}\tanh\left(\frac{z-z_{pyc}}{d_{pyc}}\right) \tag{6}$$

where z_{pyc} represents the location of the pycnocline. d_{pyc} is the thickness of the pycnocline. ρ_1 and ρ_2 represent the densities of the upper and lower fluid layers respectively. The parameters of the DJL equation are referred to LIEN et al. [32] for the measured data in the South China Sea, and the results of the DJL equation solution are shown in Fig. 4.

2.2.2 Motion simulation of the underwater vehicle

The flow field data of the ISWs solved above are used as initial values and then interpolated into the computational domain for the CFD simulations. The density change of the stratified flow is transformed into a multi-phase problem. A multi-phase, incompressible, transient flow is then solved with the CFD approach. The numerical framework consists of the Reynolds-average Navier-Stokes (RANS) equations and a *k*- ε turbulence model using standard wall functions. Velocity and pressure distributions are obtained by solving the continuity, momentum, and turbulence equations. The equations are expressed as follows:

$$\frac{\partial u_i}{\partial x_i}=0 \tag{7}$$

$$\frac{\partial}{\partial t}(\rho u_i)+\frac{\partial}{\partial x_i}(\rho u_i u_j)=\frac{\partial}{\partial x_j}\left[\mu\left(\frac{\partial u_i}{\partial x_j}+\frac{\partial u_j}{\partial x_i}\right)-\frac{2}{3}\mu\frac{\partial u_i}{\partial x_j}\right]-\frac{\partial P}{\partial x_i}+\rho g_i+F_i+\frac{\partial}{\partial x_j}\left(\overline{\rho u_i' u_j'}\right) \tag{8}$$

$$\frac{\partial}{\partial t}(\rho k)+\frac{\partial}{\partial x_i}(\rho k u_i)=\frac{\partial}{\partial x_i}\left[\left(\mu+\frac{\mu_t}{\sigma_k}\right)\frac{\partial k}{\partial x_j}\right]+G_k-\rho\varepsilon_k \tag{9}$$

$$\frac{\partial}{\partial t}(\rho\varepsilon)+\frac{\partial}{\partial x_i}(\rho\varepsilon u_i)=\frac{\partial}{\partial x_i}\left[\left(\mu+\frac{\mu_t}{\sigma_\varepsilon}\right)\frac{\partial\varepsilon}{\partial x_j}\right]+G_{1\varepsilon}\frac{\varepsilon}{k}G_\varepsilon+G_{2\varepsilon}\rho\frac{\varepsilon^2}{k} \tag{10}$$

where (7) is the continuity equation. (8) is the momentum equation. (9) and (10) are the turbulent kinetic energy *k* and turbulent dissipation rate ε equations respectively. In the above equation, *u* represents the velocity and the subscripts *i*, *j* are 1, 2, 3 respectively, which represent the *x*, *y*, *z* components of the Cartesian coordinates respectively. μ represents the dynamic viscosity of water. G_k is the turbulent kinetic energy due to the average velocity gradient. $G_{1\varepsilon}$, $G_{2\varepsilon}$, σ_k and σ_ε are all constants and take the values 1.44, 1.92, 1.0, and 1.3 respectively.

To close the above set of equations, the turbulent viscosity μ_t is introduced in place of the last term of equation (8). It is expressed as follows:

$$\mu_t=\rho C_\mu\frac{k^2}{\varepsilon} \tag{11}$$

The value of the constant C_μ is defined as 0.09. The governing equations are resolved by

numerical schemes packaging in the commercial software ANSYS Fluent. The coupled algorithm is selected. The overset framework is adopted to solve the motion of the underwater vehicle. The mixture model is used to define the vertical stratification of density in the domain. The passive motion of the SUBOFF in ISW is with 6 degrees of freedom (DOF). The gradient model for the convection and diffusion terms uses the least-squares-cell-based method. The PRESTO! scheme is used to interpolate pressure at the cell face. The second-order upwind scheme is used to solve the momentum, volume fraction, turbulent kinetic energy, and turbulent dissipation rate. The second-order implicit scheme is adopted for the temporal discretization. Second-order accuracy is thus guaranteed with the above schemes

2.3 Deep learning network

2.3.1 Architecture

Deep learning has a remarkable ability to extract complex structures from high-dimensional data. As a result, deep learning has flourished in various fields in recent years. The great success of deep learning has also boosted the development of fluid dynamics. The main application directions include the solution of physical equations, flow field reconstruction, and the prediction of related parameters, etc. A convolutional neural network (CNN) is a representative algorithm of deep learning. Based on CNN, many classical architectures have been proposed, such as ResNet, AlexNet, VGGNet, GoogleLeNet, etc. The feature extraction method in this work adopts the ResNet18 as shown in Fig. 1 (b). A residual network is made up of a series of residual blocks where the input is convolved multiple times and then added to the input. The solid and dashed lines in the Figure represent different structures. The data after feature extraction is connected to (a) and (c) respectively. In (a), the x position, y position, and the wave amplitudes of ISW are directly used as outputs. In (c), the network has two inputs. One is the signed distance function (SDF) on the underwater vehicle, and the other is the output from (b). The prediction of the flow field around the underwater vehicle is achieved by the convolutional encoder-decoder method.

2.3.2 Signed Distance Function

Conventional graphical representations such as boundaries and geometry parameters are ineffective for the cognition of deep convolutional neural networks. By using the signed distance function (SDF) to represent the geometry, Guo et al. [33] implemented feature extraction of the geometry with SDF representation and successfully achieved the prediction of the flow field. Therefore, as a two-dimensional geometric input to a deep convolutional neural network as in Fig.1 (c), the geometric representation of the SUBOFF model takes the form of an SDF. To calculate the SDF, a zero level set needs to be created as a sequence of points (i, j) in a region $\Omega \subset R^2$ that is on

the boundary of the geometry.

$$Z = \left\{(i, j) \in R^2 : f(i, j) = 0\right\} \tag{12}$$

where $f(i, j)$ is the level set function. $f(i, j) = 0$ if the point is located only at the geometric boundary, $f(i, j) < 0$ if it is inside the geometry, $f(i, j) > 0$ if it is outside the geometry.

$$D(i, j) = \min_{(i', j') \in Z} \left|(i, j) - \left(i', j'\right)\right| \operatorname{sign}(f(i, j)) \tag{13}$$

The signed distance function is defined as $D(i, j)$. Its value is determined by measuring the distance from a given point (i, j) to the nearest boundary of the closed geometry, with the sign being determined by whether (i, j) is inside or outside the geometry.

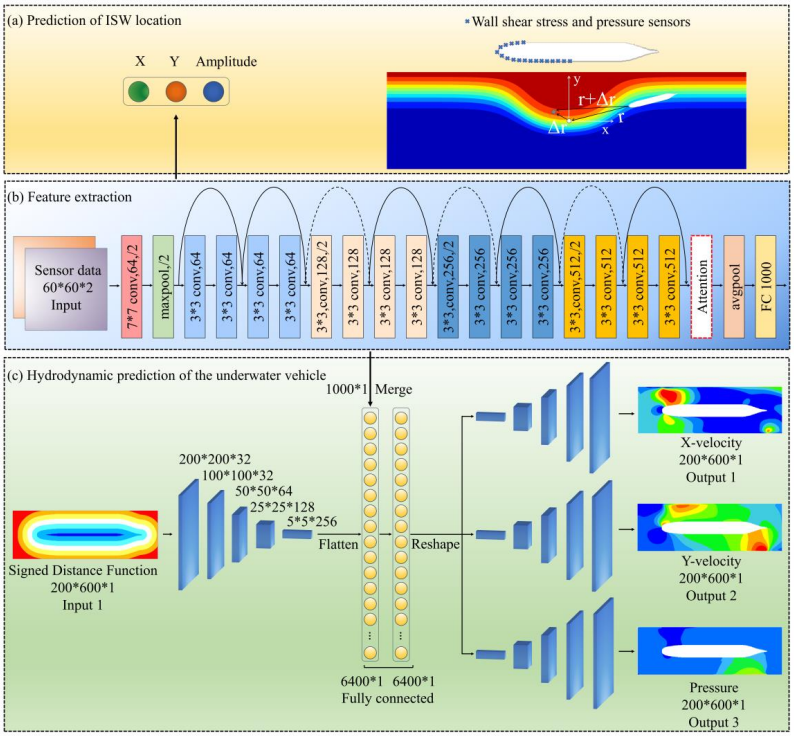

Fig. 1. Model structure of ISW detection and flow field prediction around the underwater vehicle. (a) Prediction of ISW location. (b) Feature extraction of sensor data. (c) Hydrodynamic prediction of the underwater vehicle.

3 Model verification

To verify the accuracy of the CFD calculations, dimensionless pressure coefficients

$C_P = (P_0 - P_\infty)/\rho U_\infty^2$ and dimensionless drag coefficients $C_f = \tau_w/\rho U_\infty^2$ are defined [34][35]. The details of the numerical simulations are consistent with Yang et al [36]. The zoomed view of the computational grid near the SUBOFF model is shown in Fig. 2. The obtained dimensionless pressure coefficient and dimensionless drag coefficient are compared with experimental results [37] and numerical calculations by Yang et al. [36] as shown in Fig. 3. The comparison shows that, despite slight errors at several locations, the results are in good agreement with the previous studies.

For the validation of the ISW simulation results, we choose the observations on 3 June, 2011 in the paper of Lien et al. [32] for comparison. We use the fully nonlinear DJL equation without background shear flow in the simulation. In the case of wave amplitude of 155m, we calculate the wave speed as 1.87m/s, while the calculated value in Lien [32] is 1.90m/s, and the observed value is 1.82m/s. This indicates that our simulation results are consistent with the actual ISW. The simulated ISW density contour and vertical displacement contour are shown in Fig. 4.

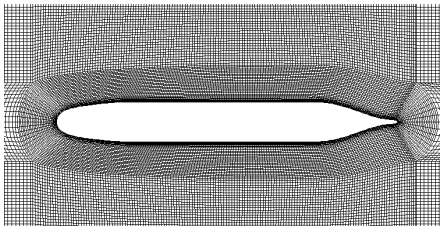

Fig. 2. Mesh near the SUBOFF model

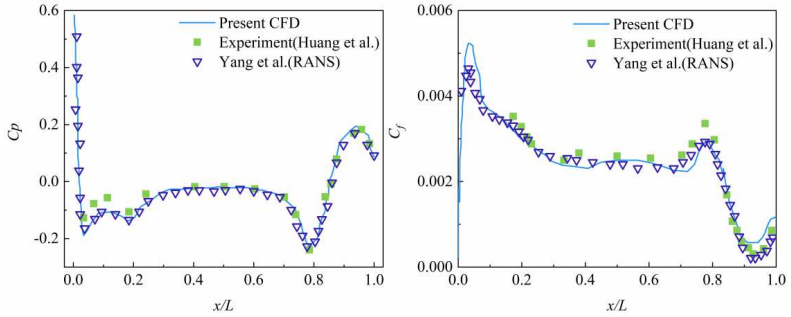

Fig. 3. Distribution of dimensionless pressure coefficient and dimensionless friction coefficient along the wall of SUBOFF

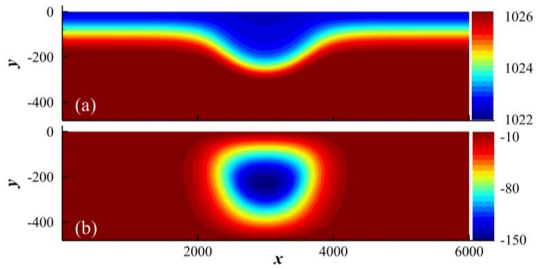

Fig. 4. ISW results of DJL solution. (a) density contour of ISW. (b) vertical displacement contour of ISW.

4 Results and discussions

4.1 Position prediction of ISW

4.1.1 Sensitivity of the predictions to the number of epochs

The number of epochs affects the accuracy of the prediction. A small number of epochs leads to the under-fitting of the prediction model due to insufficient training. A large number of epochs tends to cause overfitting and weakens the generalization ability of the model. Thus, it is important to perform sensitivity analysis on the number of epochs. To characterize the correlation between the predicted value and the real value, the Pearson's product-moment correlation coefficient is introduced. The Pearson's product-moment correlation coefficient can be defined as

$$R = \frac{\sum\left(x-m_x\right)\left(y-m_y\right)}{\sqrt{\sum\left(x-m_x\right)^2\sum\left(y-m_y\right)^2}} \tag{14}$$

where x represents the real value. y represents the predicted value. m_x and m_y are the average values of x and y, respectively. When $R > 0$, x and y are positively correlated; And when $R < 0$, x and y are negatively correlated.

The number of epochs is determined by the Pearson's product-moment correlation coefficient between the predicted and true values of x position, y position, and the absolute distance r. The change of R values when the epoch number increases from 200 to 1100 is shown in Fig. 5. The R values of the x position, y position, and the absolute distance r are the largest when the epoch is 1000. As a result, the parameter with the epoch of 1000 is selected for model training. In addition, the number and location of sensors arranged on SUBOFF are also critical to the detection of ISW and the impact of the realistic cost. In this study, the reduction in the number of sensors is achieved by dynamic mode decomposition as well as the k-means clustering method. The final number of sensors is 30 and 5, and the details of the operation are described below. The variation of the loss function with the number of epochs for sensors of 60, 30, and 5 is shown in Fig. 6. The loss function

of validation has converged to about 0.001 in the three cases, and the difference between the three is not significant. But the performance of the loss function of the training set gradually decreases with the increase in the number of sensors.

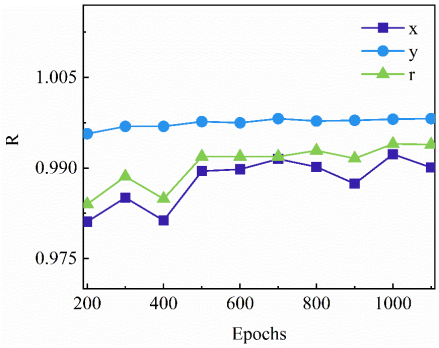

Fig. 5. The distribution of R with different numbers of epochs

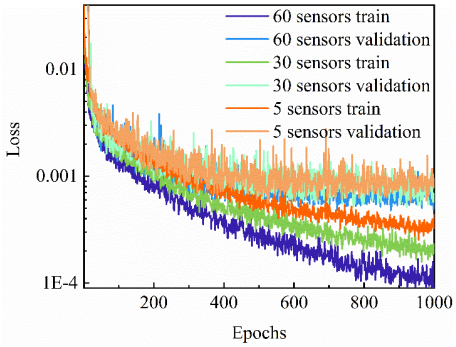

Fig. 6. Loss variation of the training and validation sets at different numbers of epochs

Fig. 7. shows the prediction accuracy using a deep learning model when the number of sensors is 60, where the truth is considered as the CFD result. (a), (b), (c) show the performance of the model in predicting the *x* position, *y* position, and the absolute distance *r*. The *R* values of the three are greater than 0.99. In general, the model performs well for the entire test dataset. In order to show the degree of deviation between the prediction and the truth, a relative error (*RE*) is introduced as in equation (15). Lines with *RE* values of 8% and 5% are plotted based on the truth. The *RE* of the predicted results of all *x* positions and *y* positions in the test dataset is within 8%, and the *RE* of the absolute distance *r* is within 5%. For the prediction at position *x*, the *RE* value increases with the increase of the distance. This is attributed to the fact that when SUBOFF is far from the trough of ISW, the extracted hydrodynamic signal is very weak, which reduces the prediction accuracy. At

position y, the predictions are uniformly distributed on both sides of $y = x$. For the prediction of the absolute length r, the results are similar to that of the x position, but the RE value is small due to the large base. (d) shows the box and whiskers plot of the RE for the different wave amplitude prediction results. The median value of RE at several wave amplitudes is around 0. The interquartile range (IQR) of the RE distribution at a wave amplitude of 170m is the smallest, which indicates the best prediction. Overall, the RE values of the upper and lower limits of the whisker are within 5%. Despite the presence of some outliers, the RE values are all within 10%.

$$RE = \frac{Prediction\ -\ Truth}{Truth} \times 100 \tag{15}$$

4.1.2 Sensor reduction based on dynamic mode decomposition

In the above studies, 60 sensors are used to collect signals for both pressure and wall shear stress. However, in the actual engineering analysis, the use of a large number of sensors will not only increase the cost and the difficulty of installation but also may make some sensors redundant due to the complex changes in the external marine environment. This is very likely to significantly compromise the prediction results. As the data measured by the sensors is time-continuous, the original data is decomposed by dynamic modal decomposition (DMD) and can be reconstructed by combining selected modes. The slowest mode tends to represent the overall trend in the data. Since the extremes of the modes often represent more drastic changes in the values at the locations of these points, this offers the possibility of sensor reduction.

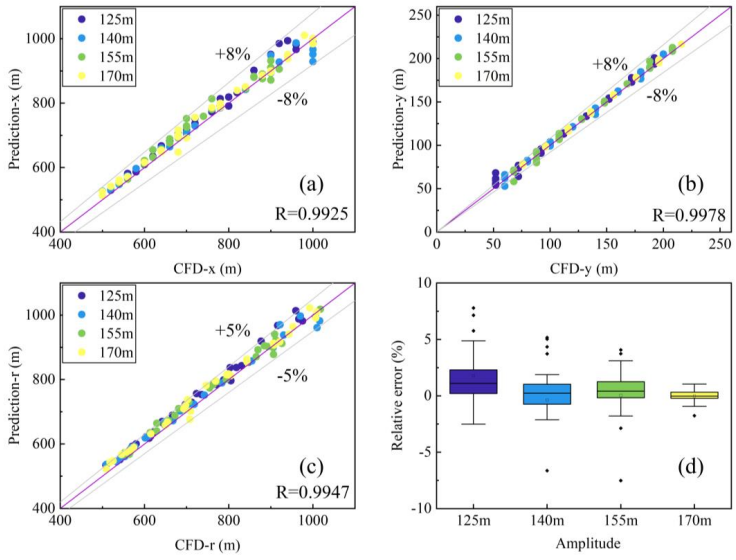

Fig. 7. Results of ISW detection when the number of pressures and wall shear stresses is 60 respectively. Prediction results of (a) position *x*; (b) position *y*; (c) absolute distance *r*; (d) amplitude.

The complete time snapshot is divided by a time step into two matrices $\mathbf{X}$, $\mathbf{X}'$.

$$\begin{aligned}\mathbf{X} &= \begin{bmatrix}\mathbf{x}_1 & \mathbf{x}_2 & \cdots & \mathbf{x}_{m-1}\end{bmatrix} \\ \mathbf{X}' &= \begin{bmatrix}\mathbf{x}_2 & \mathbf{x}_3 & \cdots & \mathbf{x}_m\end{bmatrix}\end{aligned} \tag{16}$$

Assuming that $\mathbf{X}$ is linearly correlated with $\mathbf{X}'$, we can obtain the matrix $\mathbf{A}$. The A matrix can be calculated by eigendecomposition $\mathbf{A}\boldsymbol{\Phi} = \boldsymbol{\Phi}\boldsymbol{\Lambda}$. This step is obtained based on the low-rank approximation of the data matrix.

$$\mathbf{X}' = \mathbf{A}\mathbf{X} \tag{17}$$

Eigenvalues and eigenvectors are obtained utilizing rank truncation. These eigenvalues move forward in time. The state at each time in the original data can be calculated by the linear combination of DMD modes (columns ϕ_k of $\boldsymbol{\Phi}$), eigenvalues ($\lambda_k = \Lambda_{kk}$), and corresponding modal amplitudes b:

$$\mathbf{x}_k = \boldsymbol{\Phi}\boldsymbol{\Lambda}^k\mathbf{b} \tag{18}$$

Another expression in the continuous time-setting is to scale the eigenvalues $\omega_k = \dfrac{\log \lambda_k}{i\Delta t}$:

$$\mathbf{x}(t) = \sum_{k=1}^{r} b_k \phi_k(\xi)\exp(i\omega_k t) \tag{19}$$

The multiresolution DMD (mrDMD) method overcomes the common shortcomings of traditional DMD. It provides a hierarchical time sampling framework, which can recursively represent different time scale phenomena. On the one hand, mrDMD can be used to analyze the time and location of high-frequency information. On the other hand, it defines slow mode, which can be used to determine the basic trend of the dataset. Two parameters need to be defined first with this method, the number of levels *L* and the removal radius ρ. At each level, the maximum number of time bins $j_{\max}$ is 2^{l-1}. The removal radius is defined as the radius of the circle in the complex plane. The mode corresponding to the eigenvalue within the radius is the slow mode. In this study, $\rho = 2/T$ is defined, where T stands for the length of time bins. To clearly represent the solutions corresponding to each level of $\mathbf{x}_{\text{mrDMD}}(t)$, we define the following functions.

$$f_{\ell,j}(t) = \begin{cases}1, & t \in \left[t_j, t_{j+1}\right] \\ 0, & \text{elsewhere}\end{cases} \text{ with } j = 1, 2, \ldots, 2^{(\ell-1)} \tag{20}$$

where $f_{\ell,j}(t)$ is non-zero only in the time bin to be solved. Therefore, from the solution formula of DMD above, the solution formula of mrDMD can be extended as:

$$\mathbf{x}_{\text{mrDMD}}(t) = \sum_{\ell=1}^{L}\sum_{j=1}^{J}\sum_{k=1}^{m_\ell} f_{\ell,j}(t) b_k^{(\ell,j)} \phi_k^{(\ell,j)}(\xi)\exp\left(i\omega_k^{(\ell,j)} t\right) \tag{21}$$

Accepted to Phys. Fluids 10.1063/5.0123365

The sensors are placed at equal intervals on the surface of the SUBOFF model as in Fig. 11. The pressure and wall shear stresses are monitored. In Fig. 8, we perform mrDMD analysis for the data measured by shear stress sensors at different locations with 240 snapshots. The time interval between every two temporal snapshots is 0.1s, corresponding to the data sampling time of 6s in the previous deep learning networks. The maximum level of mrDMD is chosen to be 4, so the maximum level corresponds to 8 time bins, each containing 30 snapshots. (a) shows the variation of the original data over time and (b) shows the reconstruction results of mrDMD. We find that the reconstructed results are highly consistent with the original results. (c), (d), (e) and (f) denote level 1, level 2, level 3, and level 4 respectively. Likewise, Fig. 9 shows the results of the mrDMD decomposition of the pressure data. Compared to the wall shear stress, we find that the pressure variation is simpler. From the distribution of the low-frequency modes of level1 shown in (c), the overall trend of pressure variation is gradually increasing at all locations. The changes are more dramatic in the head and tail of the underwater vehicle. Although some details are missed for the reconstructed signals of the four levels due to the strong nonlinearity, the principal of the data can still be obtained. For better quality of the reconstruction, increasing the number of levels is perfectly possible. In this work, only the slow modes are needed, which are the main part of the data occupied from the level of decomposition.

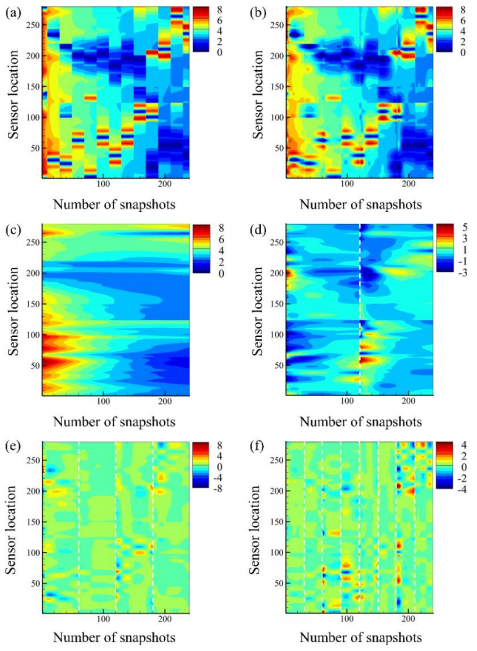

Fig. 8. Results of mrDMD decomposition of wall shear stress. (a) Original data. (b) Reconstructed

data. (c) Level 1 results after decomposition. (d) Level 2 results after decomposition. (e) Level 3 results after decomposition. (f) Level 4 results after decomposition.

By defining the removal radius ρ, the slowest modes corresponding to all data sets are found. The mean mode distribution of the pressure and wall shear stress on the wall of the SUBOFF is shown in Fig. 10. A similar trend in the mean mode variation of the pressure and wall shear stress can be found. Moreover, the fluctuation of the mean mode of the wall shear stress is more dramatic. The sorting should not include the mean modes behind the appendages of the underwater vehicle. And the sensor positions with the first 30 mode values are selected, resulting in a new arrangement with reduced sensors. The sensor arrangement for pressure and wall shear stress selected by the DMD mode is shown in Fig. 11. The sensors at these locations are less susceptible to noise interference as the values vary widely when data acquisition is performed. However, the spacing between two sensors in this arrangement is still relatively small, and a large amount of similar data will be acquired. Therefore, k-means clustering methods are necessary to implement, which will be described in the following section.

The detection results of the ISW after sensor reduction are shown in Fig. 12. The prediction results from the x position are similar to those without sensor reduction. The prediction accuracy becomes progressively worse as the distance increases. With the decrease in the number of sensors, however, it is found that the linearity of the prediction results for the true values becomes worse and the distance of the discrete points from $y = x$ increases. We can also find this phenomenon in the change in the value of R. Despite the slight decrease in accuracy, the prediction quality is still very positive. For the prediction of the y position, the accuracy increases slightly, and the R value changes from 0.9978 to 0.9987. The prediction of the absolute length r is more influenced by the x position because of the larger value of the x position. The predicted R value of the absolute length is 0.9933. The distribution of the RE values of the wave amplitude does not differ much from that without sensor reduction. However, the RE values of the abnormal points in (d) are much larger, especially for the wave amplitude of 140m. But the RE values are all within 10%, in other words, the prediction accuracy can still reach 90%.

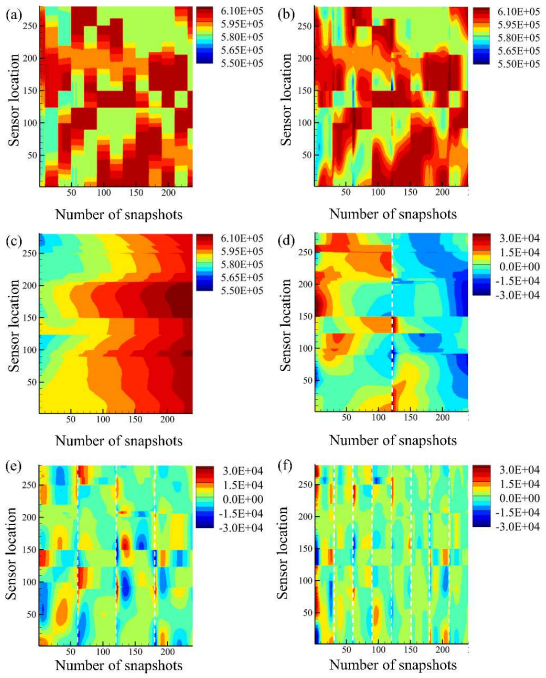

Fig. 9. Results of mrDMD decomposition of pressure (a) Original data. (b) Reconstructed data. (c) Level 1 results after decomposition. (d) Level 2 results after decomposition. (e) Level 3 results after decomposition. (f) Level 4 results after decomposition.

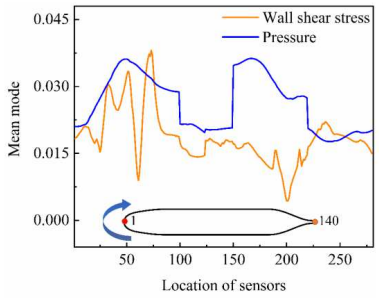

Fig. 10. Distribution of the mean modal values along the surface of the SUBOFF model

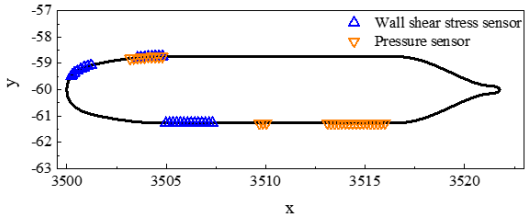

Fig. 11. The position of the pressure and wall shear stress sensors after reduction using DMD

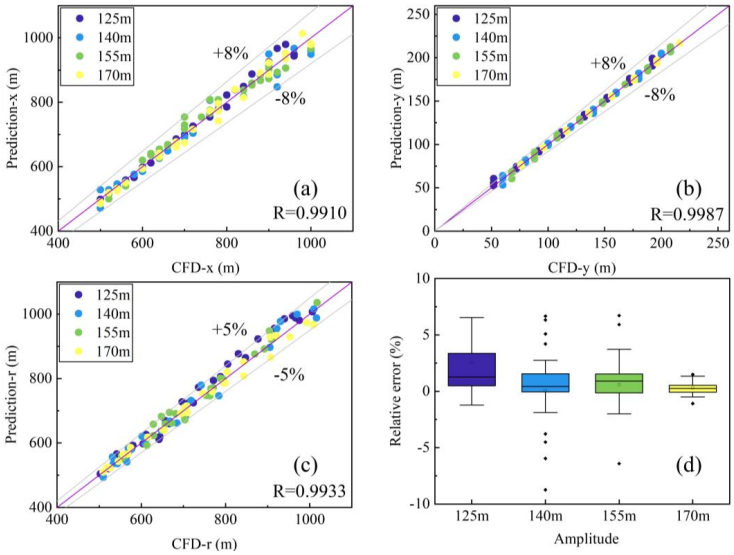

Fig. 12. Results of ISW detection when the number of pressure and wall shear stress sensors is 30 respectively. Prediction results of (a) position x. (b) position y. (c) absolute distance. (d) amplitude.

4.1.3 Sensor reduction based on k-means clustering method

From the above, it can be seen that the distance between two sensors is too small from the obtained sensor arrangement method, despite the sensor reduction using the DMD method. This can result in an arrangement of sensors that will have many extremely similar time series signals, which can lead to redundancy in the input information. Given this problem, a k-means clustering method to cluster analysis is used to discard redundant sensor locations and achieve sensor sparsity. The traditional k-means clustering method uses Euclidean distance for clustering. The Euclidean distance is defined by equation (19), where $A=\langle a_1,\ldots,a_r\rangle$ and $B=\langle b_1,\ldots,b_r\rangle$ are two time series. s is the distance corresponding to the corresponding element (or coordinate) in the sequence.

However, the Euclidean distance method is suitable for the change of the *y*-axis, but not for the change of the time axis, which makes the clustering results very different from the actual situation.

Therefore, the dynamic time warping (DTW) method is introduced. The corrected distance is calculated as follows.

$$D(A,B)=\sqrt{\delta\left(a_1,b_1\right)^2+\cdots+\delta\left(a_T,b_T\right)^2} \tag{22}$$

$$D\left(A_i,B_j\right)=\delta\left(a_i,b_j\right)+\min\begin{Bmatrix}D\left(A_{i-1},B_{j-1}\right)\\D\left(A_i,B_{j-1}\right)\\D\left(A_{i-1},B_j\right)\end{Bmatrix} \tag{23}$$

We select the time series of pressure and wall shear stress after DMD sensor reduction. The 30 time series objects for all wall shear stresses are shown in Fig. 13 (a). Each object consists of 60 time stamps, and the objects in the same cluster exhibit a pattern similar to that of 4 consecutive time stamps. According to the above, the 30 time series are divided into 5 clusters, as shown in (b), (c), (d), (e), and (f). We find that the patterns of the first four clusters show a uniform trend over time despite the difference in the magnitude of the changes. The difference between the values of the wall shear stress at the initial moment and the end moment of cluster 5 is much larger. Consistent with the operation of wall shear stress, we obtain the results of pressure clustering, as shown in Fig. 14. During the first 1s, the signals measured by all arranged pressure sensors exhibit strong fluctuations. This is due to the fact that at the beginning the underwater vehicle is in a non-stable state. As the pitch angle increases, the value of the pressure increases steadily. The related conclusion can be corroborated by the (c) in Fig 9, which exhibits the low-frequency modal distribution and represents the overall development of the data. Therefore, one location in each cluster is picked for sensor placement. The final arrangement on SUBOFF is shown in Fig. 15.

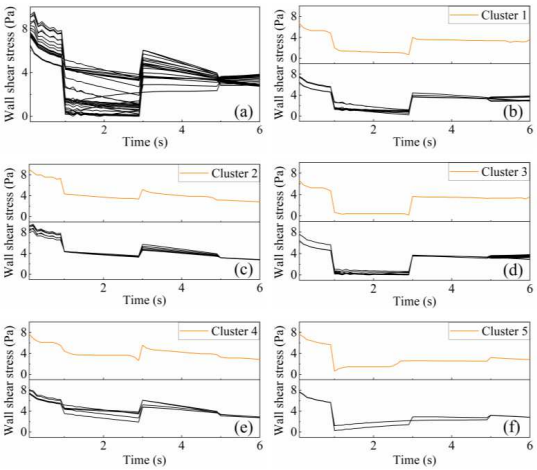

Fig. 13. Clustering results of wall shear stress data. (a) Original data. Clustering results of (b) cluster 1; (c) cluster 2; (d) cluster 3; (e) cluster 4; (f) cluster 5.

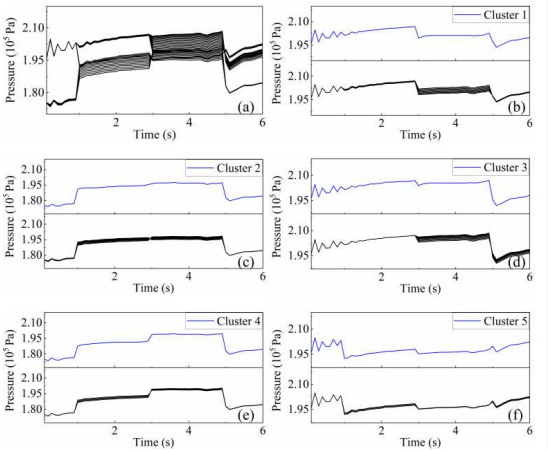

Fig. 14. Clustering results of pressure data. (a) Original data. Clustering results of (b) cluster 1; (c) cluster 2; (d) cluster 3; (e) cluster 4; (f) cluster 5.

After the k-means method for clustering, we obtained the sparse arrangement of pressure and wall shear stress sensors. The detection results of the ISW are obtained according to the arrangement scheme of the sparse sensors, as shown in Fig. 16. The prediction results of the *x* position are worse than that of the 30 sensors. The difference in performance is particularly apparent when the distance of *x* is small. When the *R* value is used as a criterion, the predicted *R* value at position *x* is reduced to 0.9850. The predicted *R* value at position *y* remains unchanged. The *R* value of the absolute distance prediction result also decreases accordingly, from 0.9947 to 0.9933. A box plot of the *RE* values according to the wave amplitude is shown in (d). Here the distance between the upper and lower limits of the box plot is greater. The *RE* with a wave amplitude of 170m is the smallest.

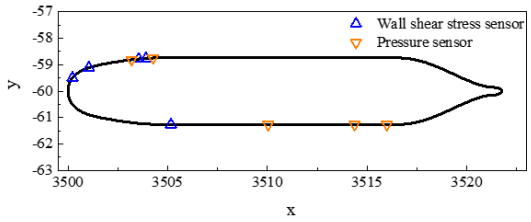

Fig. 15. The position of the pressure and wall shear stress sensors after reduction using the k-means clustering method

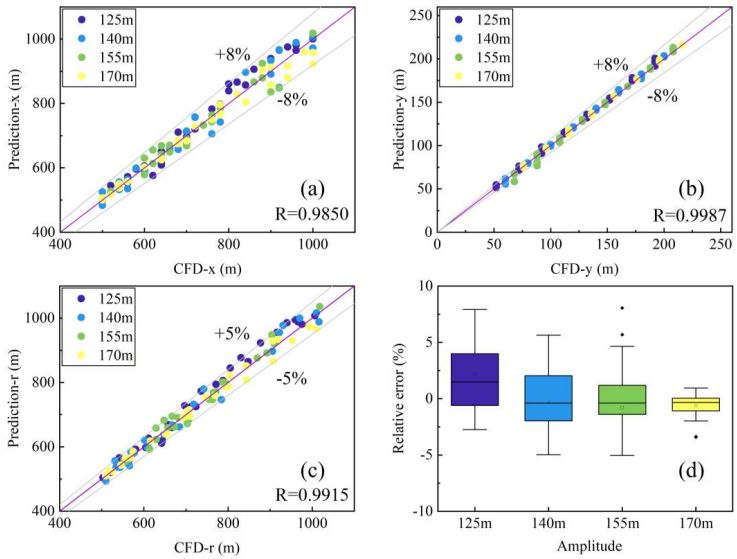

Fig. 16. Results of ISW detection when the number of sensors for pressure and wall shear stress is 5. Prediction results of (a) position x. (b) position y. (c) absolute distance. (d) amplitude.

4.2 Prediction of the flow field around the underwater vehicle

With the influences of the ISWs, the attitude of the underwater vehicle will be changed. In addition, the incoming flow conditions are different when the underwater vehicle is in different positions of the ISW. As a result, the flow field around the underwater vehicle is complex. If the surrounding flow field of the underwater vehicle is successfully predicted, it is very useful for its attitude adjustment. Consequently, this study designs a deep learning network for predicting the surrounding flow field of the underwater vehicle after completing ISW detection. The specific structure of the network is shown in Fig. 1 (c). The feature extraction part is consistent with the one used in (a), as shown in (b). In the field of digital image processing, Woo [38] proposed the convolutional block attention module (CBAM). CBAM is an attention mechanism module that combines spatial and channel attention, which can achieve better results in the classification domain compared to traditional channel attention. To achieve better predictions, CBAM is added in Fig. 1 (b) and the effect of CBAM on the prediction results is analyzed.

Fig. 17 shows the predicted results of the flow field around the underwater vehicle for different cases. The predicted pressure uses p- ρgh, where p stands for the static pressure. The Figure shows the prediction results of the flow field with 60 sensors when no attention mechanism is added, and 60, 30, and 5 sensors when the attention mechanism is added. The comparison of the flow field

prediction results under different conditions shows that the prediction results of U and V are good, and the prediction results of pressure are slightly worse than the U and V. For the global error analysis, we choose the L_2 error norm for characterization, where x represents the true value and y represents the predicted value.

$$L_2(x, y) = \|x - y\|_2 / \|x\|_2 \tag{24}$$

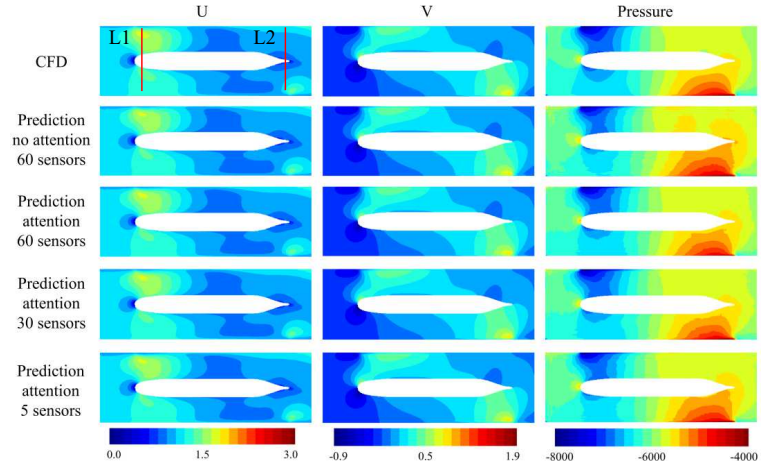

Fig. 17. Flow field prediction with different network structures

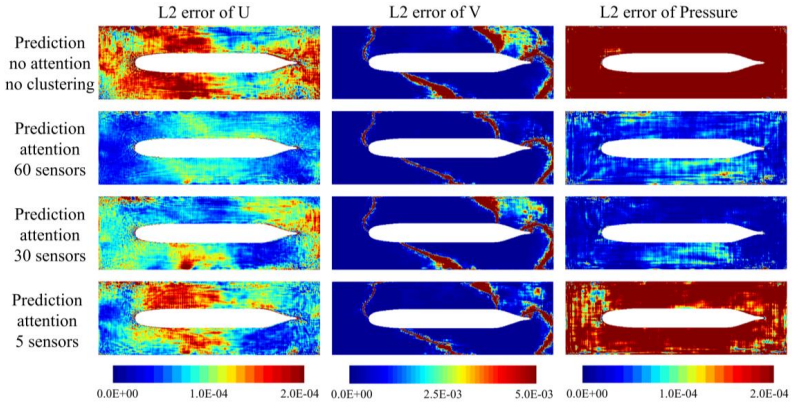

Fig. 18. L_2 error of flow field prediction under different network structures

From the L_2 error distribution in Fig. 18, it can be found that the worst prediction is achieved when no attention mechanism is added to the network framework. With the attention mechanism, the prediction becomes progressively worse as the number of sensors decreases. Changing the

condition has little effect on the L_2 error of V prediction results. Compared to the predicted results for U and V, the predicted results for pressure are slightly worse when the number of sensors is reduced to 5. To quantitatively represent the accuracy of the global prediction, we introduce structural similarity (SSIM) and peak signal-to-noise ratio (PSNR). In this study, SSIM is used to measure the similarity of the predicted results to the CFD results. SSIM values range from -1 to 1, the closer to 1 the better the prediction is. SSIM is defined as follows:

$$\mathrm{SSIM}(x,y)=\frac{\left(2\mu_x\mu_y+C_1\right)\left(2\sigma_{xy}+C_2\right)}{\left(\mu_x^2+\mu_y^2+C_1\right)\left(\sigma_x^2+\sigma_y^2+C_2\right)} \tag{25}$$

where x and y represent the true and predicted value. μ_x and μ_y are the mean of x and y. σ_x^2 and σ_y^2 are the standard deviation of x and y. σ_{xy} is the cross-covariance of x and y.

PSNR is often defined simply by mean square error (MSE). As the MSE approaches 0, the PSNR approaches infinity. Therefore, a larger PSNR indicates a better prediction.

$$\mathrm{PSNR}\left(x,y\right)=20\log_{10}\left(\frac{1}{\sqrt{MSE\left(x,y\right)}}\right) \tag{26}$$

Based on the several settings above, the PSNR and SSIM histograms for several cases are shown in Fig. 19. According to the distribution of PSNR, we can find the smallest PSNR value when no attention mechanism is added compared with other conditions. Moreover, the PSNR value of p is drastically affected by different network structures. The prediction performance is the best when the number of sensors is 60 and gradually decreases as the number of sensors decreases. From the distribution of SSIM values, we can find that the prediction accuracy does not differ much for U and V with different network structures. The prediction of p is as susceptible to the influence of network structure as the PSNR values.

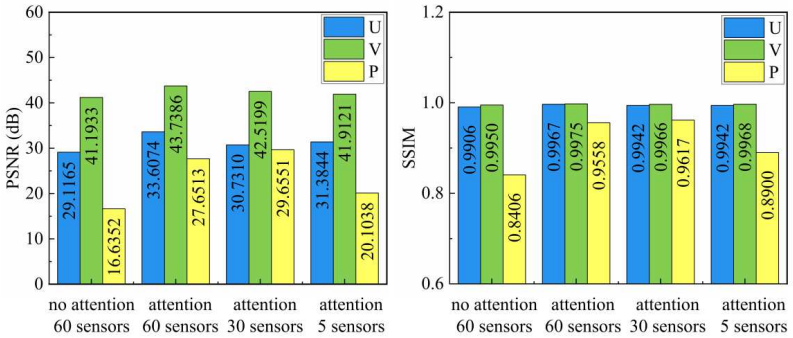

Fig. 19. Comparison of SSIM and PSNR values under different network structures

The above are all predictions of performance from the overall analysis of the flow field. In the

following, we present a quantitative analysis of the local predictive performance. The predicted performance for different conditions was compared by extracting data above two vertical lines at the head and tail of the underwater vehicle, as shown in Fig. 17. Similar to the global analysis results, it shows good agreement between the CFD results and the predictions under each condition for U and V, as shown in Fig. 20. For the prediction of p, the overall trend of the prediction results for each condition is consistent with CFD. However, the degree of deviation of the prediction results from CFD under various conditions is different. Consistent with the results of the above global analysis, the results of adding the attention mechanism outperform those without it, and those with more sensors outperform those with fewer sensors. Nevertheless, the prediction results are satisfactory with the addition of an attention mechanism with 5 sensors each for pressure and wall shear stress.

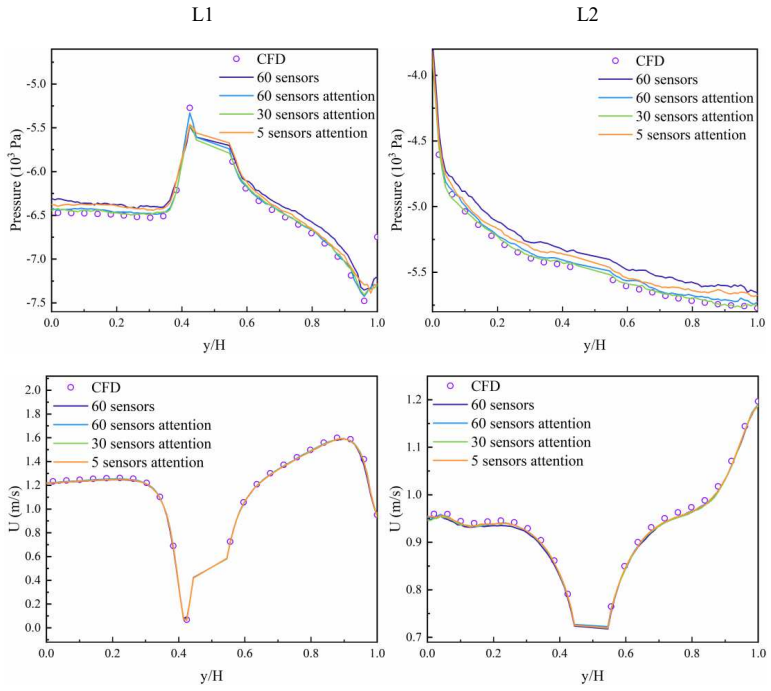

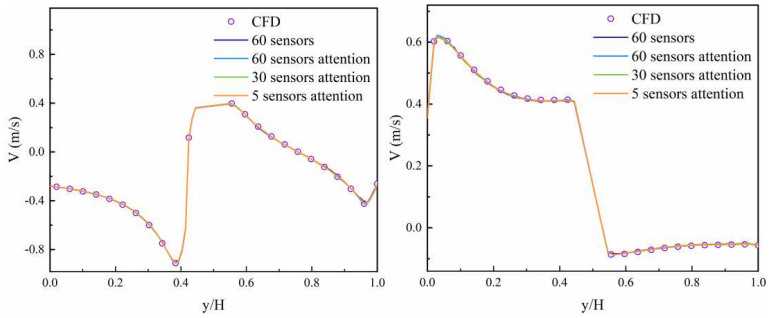

Fig. 20. Detailed comparison of values on L1 and L2 (L1 and L2 are the two vertical lines at the head and tail of the underwater vehicle, and their distribution is shown in FIG. 17.)

5 Conclusions

This study presents a method based on a deep convolution neural network to detect ISW. Through accurate numerical simulations of the free underwater vehicle interacting with the ISWs, detection data on the corresponding sensors are obtained. The input and output databases under various operating conditions are established. An effective deep learning algorithm is established to realize the accurate detection of ISW.

A residual neural network based on Resnet 18 is built. Here, the data collected by the sensor is pre-processed accordingly and converted into a two-channel image type data as input. The relative position of the underwater vehicle to the ISW is used as an output (including x, y, absolute length as well as wave amplitude). The prediction accuracy of ISW can reach 95%.

To obtain the mean mode (representing the overall framework of data variation), the dynamic mode decomposition (DMD) method is used. The number of sensors is reduced by selecting the position with the largest mean mode, which can effectively avoid the interference of noise. The number of sensors is reduced from 60 to 30, while the accuracy is slightly reduced in terms of the relative error distribution as well as the distribution of linear correlation coefficients. The k-means clustering method is chosen so that the sensor distribution becomes further sparse. The final number of sensors is reduced to 5. The results show that its prediction accuracy is slightly worse than the first two. However, the accuracy can still reach 92%.

The prediction of the flow field around the underwater vehicle is achieved by combining autoencoder, Resnet18, and SDF methods, which provide important information for the following attitude adjustment operations. Through quantitative analysis of L_2 error, PSNR, and SSIM metrics, the prediction results under different conditions are compared. The results show that the prediction results are better with the addition of the attention mechanism, and the performance becomes worse

with a smaller number of sensors.

In summary, this work proposes a novel hydrodynamic detection method based on machine learning. The method can complement the existing detection techniques and guarantee the safety of underwater vehicles, which has important engineering prospects.

Acknowledgments

This research was supported by the National Natural Science Foundation of China (No. 52201380, 52101373), Shaanxi Provincial Key R&D Program (No. 2021KW-38), Qinchuangyuan high-level innovative and entrepreneurial talents introduction plan (No. QCYRCXM-2022-125), Major Science and Technology Projects in Henan Province (No. 201400211100), and Fundamental Research Funds for the Central Universities (No. 3102021HHZY030009).

Declaration of competing interest

The authors declare that they have no known competing financial interests or personal relationships that could have appeared to influence the work reported in this paper.

Availability of data

The data that support the findings of this study are available from the corresponding author upon reasonable request.

Reference

[1] Huang, X., Chen, Z., Zhao, W., Zhang, Z., Zhou, C., Yang, Q., & Tian, J. (2016). An extreme internal solitary wave event observed in the northern South China Sea. Scientific reports, 6(1), 1-10.

[2] Sarkar, S., & Scotti, A. (2017). From topographic internal gravity waves to turbulence. Annual Review of Fluid Mechanics, 49, 195-220.

[3] Wang, X., & Zhou, J. F. (2021). Numerical and experimental study of internal solitary wave loads on tension leg platforms. Journal of Hydrodynamics, 33(1), 93-103.

[4] Xu, J., Wang, L. L., Tang, H. W., Hai, Z., & Williams, J. J. R. (2019). Scalar transport by propagation of an internal solitary wave over a slope-shelf. Journal of Hydrodynamics, 31(2), 317-325.

[5] Zou, L., Wen, Z., Sun, T., Ma, X., & Wang, X. (2021). Experimental study on transformation and energy properties of depression internal solitary wave over a bottom step. Physics of Fluids, 33(3), 032109.

[6] Li, S., Yu, C., Qian, S., Song, J., & Cao, A. (2021). Interfacial waves modulated by linear shear flow of the upper layer in a two-layer fluid with arbitrary layer depths. Physics of Fluids, 33(4),

042112.

[7] Ding, W., Ai, C., Jin, S., & Lin, J. (2020). Numerical investigation of an internal solitary wave interaction with horizontal cylinders. Ocean Engineering, 208, 107430.

[8] Wang, Y., Wang, L., Zhu, H., Tang, H., & Wei, G. (2016). A numerical study of the forces on two tandem cylinders exerted by internal solitary waves. Mathematical Problems in Engineering, 2016.

[9] Cheng, M. H., Hwang, R. R., & Hsieh, C. M. (2020). Numerical study on the transformation of an internal solitary wave propagating across a vertical cylinder. Applied Ocean Research, 95, 102016.

[10] Li, J., Zhang, Q., & Chen, T. (2021). Numerical Investigation of Internal Solitary Wave Forces on Submarines in Continuously Stratified Fluids. Journal of Marine Science and Engineering, 9(12), 1374.

[11] Wang, S. D., Wei, G., Du, H., Wu, J. L., & Wang, X. L. (2020). Experimental investigation of the wave-flow structure of an oblique internal solitary wave and its force exerted on a slender body. Ocean Engineering, 201, 107057.

[12] He, G., Xie, H., Zhang, Z., & Liu, S. (2022). Numerical Investigation of Internal Solitary Wave Forces on a Moving Submarine. Journal of Marine Science and Engineering, 10(8), 1020.

[13] Zou, P. X., Bricker, J. D., & Uijttewaal, W. S. (2021). The impacts of internal solitary waves on a submerged floating tunnel. Ocean Engineering, 238, 109762.

[14] Chen, M. , Ke, C. , You, Y. X. , & Yu, H. T. (2018). Experimental study of forces on a multi-column floating platform in internal solitary waves. Applied Ocean Research, 78, 192–200.

[15] Alpers, W. (1985). Theory of radar imaging of internal waves. Nature, 314(6008), 245-247.

[16] Caponi, E. A., Crawford, D. R., Yuen, H. C., & Saffman, P. G. (1988). Modulation of radar backscatter from the ocean by a variable surface current. Journal of Geophysical Research: Oceans, 93(C10), 12249-12263.

[17] Liu, A.K., Ramp, S.R., Zhao, Y.H., Tang, T.Y., (2004). A case study of internal solitary wave propagation during ASIAEX 2001. IEEE J. Ocean. Eng. 29, 1144–1156.

[18] Magalhaes, J. M., Da Silva, J. C. B., & Buijsman, M. C. (2020). Long lived second mode internal solitary waves in the Andaman Sea. Scientific Reports, 10(1), 1-10.

[19] Bai, X., Li, X., Lamb, K. G., & Hu, J. (2017). Internal solitary wave reflection near Dongsha atoll, the South China Sea. Journal of Geophysical Research: Oceans, 122(10), 7978-7991.

[20] Tensubam, C. M., Raju, N. J., Dash, M. K., & Barskar, H. (2021). Estimation of internal solitary wave propagation speed in the Andaman Sea using multi–satellite images. Remote Sensing of Environment, 252, 112123.

[21] Lien, R. C., Tang, T. Y., Chang, M. H., & d'Asaro, E. A. (2005). Energy of nonlinear internal

waves in the South China Sea. Geophysical Research Letters, 32(5).

[22] Alford, M. H., Lien, R. C., Simmons, H., Klymak, J., Ramp, S., Yang, Y. J., ... & Chang, M. H. (2010). Speed and evolution of nonlinear internal waves transiting the South China Sea. Journal of Physical Oceanography, 40(6), 1338-1355.

[23] Ramp, S. R., Yang, Y. J., & Bahr, F. L. (2010). Characterizing the nonlinear internal wave climate in the northeastern South China Sea. Nonlinear Processes in Geophysics, 17(5), 481-498.

[24] Li, Q., & Farmer, D. M. (2011). The generation and evolution of nonlinear internal waves in the deep basin of the South China Sea. Journal of Physical Oceanography, 41(7), 1345-1363.

[25] Huang, X., Chen, Z., Zhao, W., Zhang, Z., Zhou, C., Yang, Q., & Tian, J. (2016). An extreme internal solitary wave event observed in the northern South China Sea. Scientific reports, 6(1), 1-10.

[26] Wolf, B. J., Pirih, P., Kruusmaa, M., & Van Netten, S. M. (2020). Shape classification using hydrodynamic detection via a sparse large-scale 2D-sensitive artificial lateral line. IEEE Access, 8, 11393-11404.

[27] Lakkam, S., Balamurali, B. T., & Bouffanais, R. (2019). Hydrodynamic object identification with artificial neural models. Scientific reports, 9(1), 1-12.

[28] Wolf, B. J., van de Wolfshaar, J., & van Netten, S. M. (2020). Three-dimensional multi-source localization of underwater objects using convolutional neural networks for artificial lateral lines. Journal of the Royal Society Interface, 17(162), 20190616.

[29] Liu, G., Gao, S., Sarkodie-Gyan, T., & Li, Z. (2018). A novel biomimetic sensor system for vibration source perception of autonomous underwater vehicles based on artificial lateral lines. Measurement Science and Technology, 29(12), 125102.

[30] Liu, G., Liu, S., Wang, S., Hao, H., & Wang, M. (2019). Research on artificial lateral line perception of flow field based on pressure difference matrix. Journal of Bionic Engineering, 16(6), 1007-1018.

[31] Deepwell, D., Clarry, C., Subich, C., & Stastna, M. (2021). Vortex generation due to internal solitary wave propagation past a sidewall constriction. Journal of Fluid Mechanics, 913.

[32] Lien, R. C., Henyey, F., Ma, B., & Yang, Y. J. (2014). Large-amplitude internal solitary waves observed in the northern South China Sea: properties and energetics. Journal of Physical Oceanography, 44(4), 1095-1115.

[33] Guo, X., Li, W., & Iorio, F. (2016, August). Convolutional neural networks for steady flow approximation. In Proceedings of the 22nd ACM SIGKDD international conference on knowledge discovery and data mining (pp. 481-490).

[34] Wang, C., Du, W, Li, G. H., Du, P., Hu, H.B. (2022). Numerical simulation of influence of ocean internal waves on hydrodynamic characteristics of underwater vehicles. Chinese Journal of

Ship Research, 17(3), 102-111.

[35] Chen, J. J., Pan, Z. Y., Zheng, W. T., Chen, M., Xia, X., Xiao, D. L. (2021). Research on hydrodynamic characteristics of underwater vehicle with X-rudder configuration coupling with incidence and rudder angle. Chinese Journal of Ship Research, 17, 1-9.

[36] Yang, C., & Lohner, R. (2003, September). Prediction of flows over an axisymmetric body with appendages. In The 8th International Conference on Numerical Ship Hydrodynamics, Busan, Korea.

[37] Liu, H. L., & Huang, T. T. (1998). Summary of DARPA SUBOFF experimental program data. NAVAL SURFACE WARFARE CENTER CARDEROCK DIV BETHESDA MD HYDROMECHANICS DIRECTORATE.

[38] Woo, S., Park, J., Lee, J. Y., & Kweon, I. S. (2018). Cbam: Convolutional block attention module. In Proceedings of the European conference on computer vision (ECCV) (pp. 3-19).

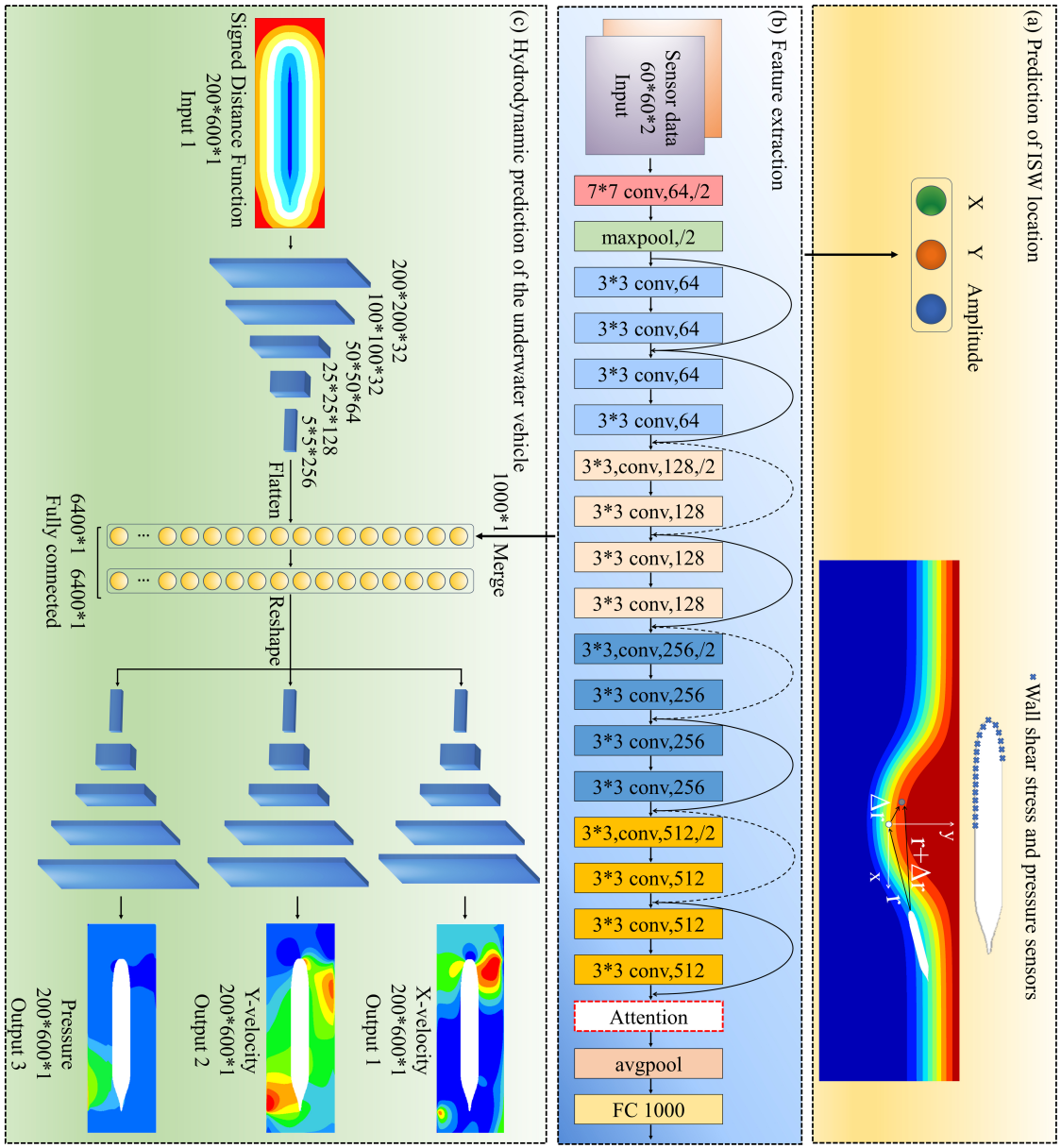

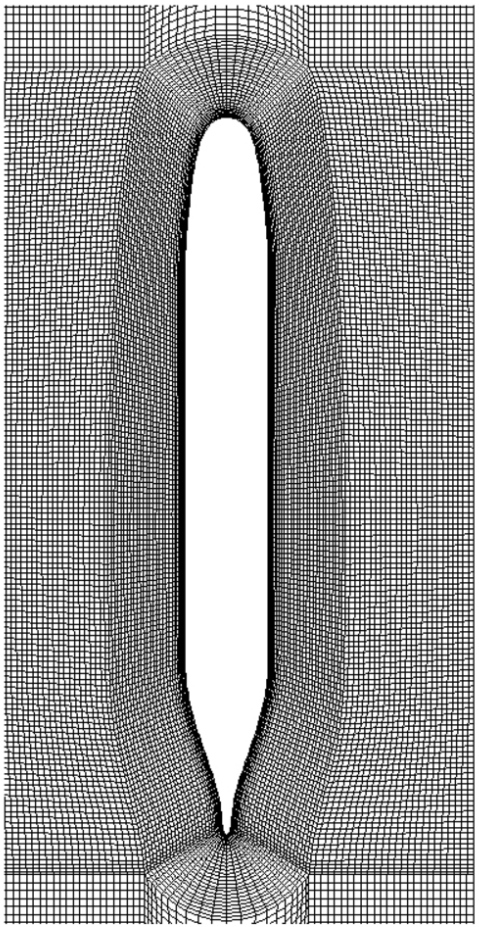

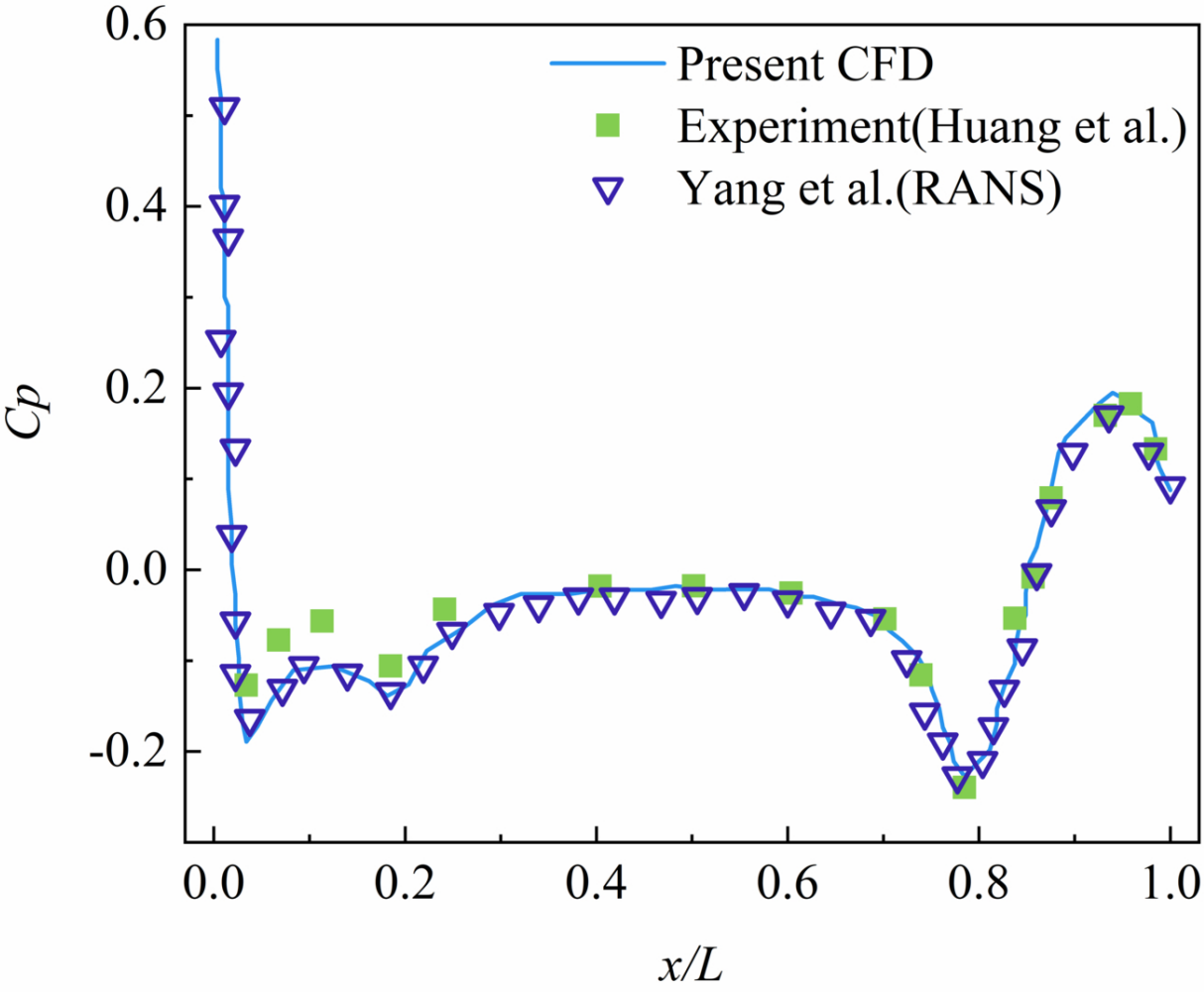

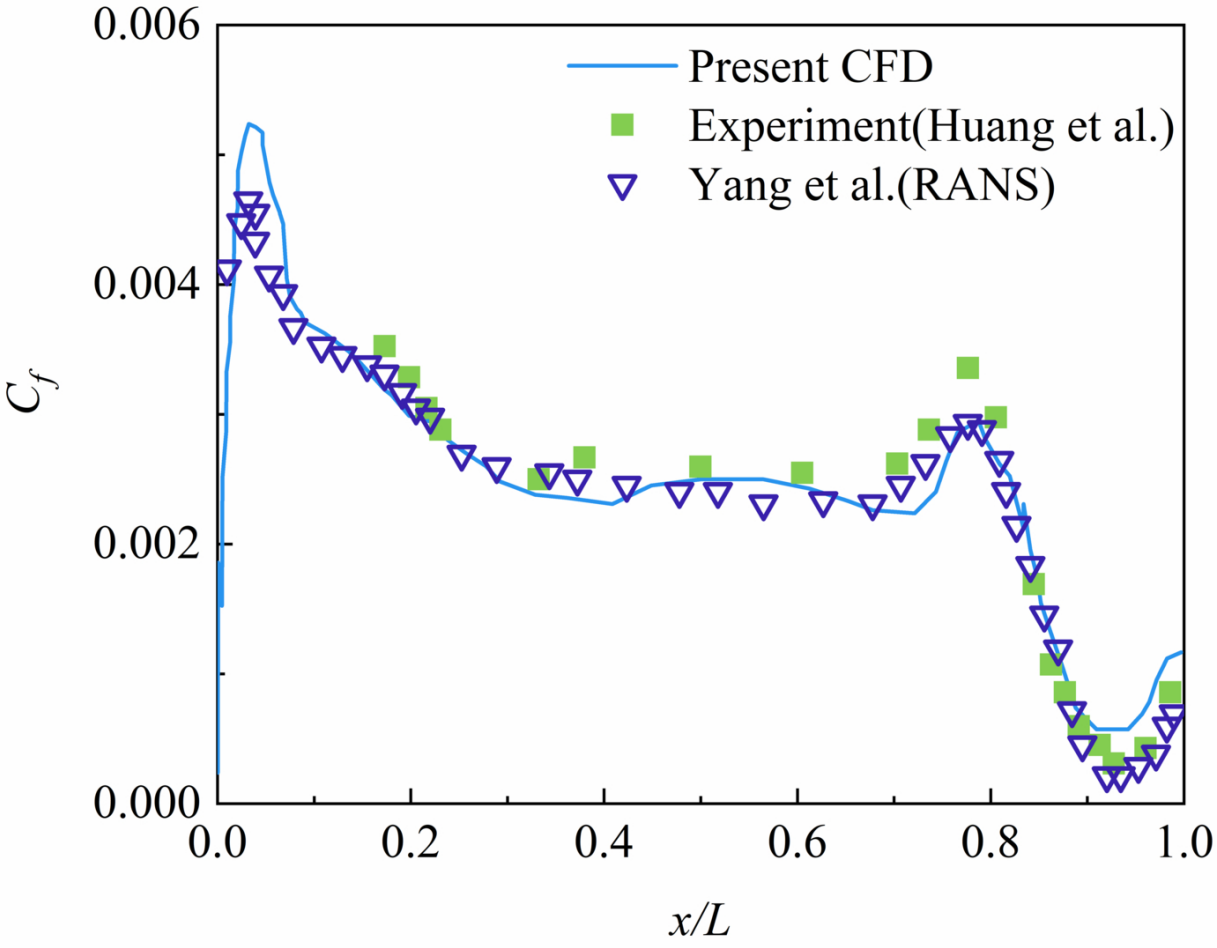

PLEASE CITE THIS ARTICLE AS DOI: 10.1063/5.0123365

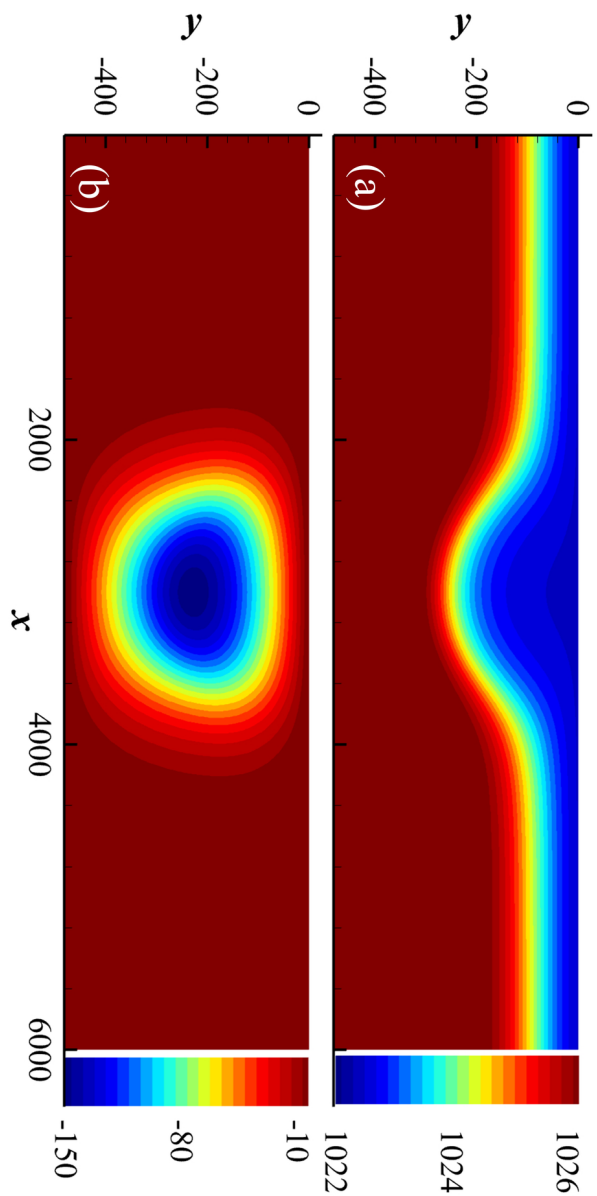

Physics of Fluids

PLEASE CITE THIS ARTICLE AS DOI: 10.1063/5.0123365

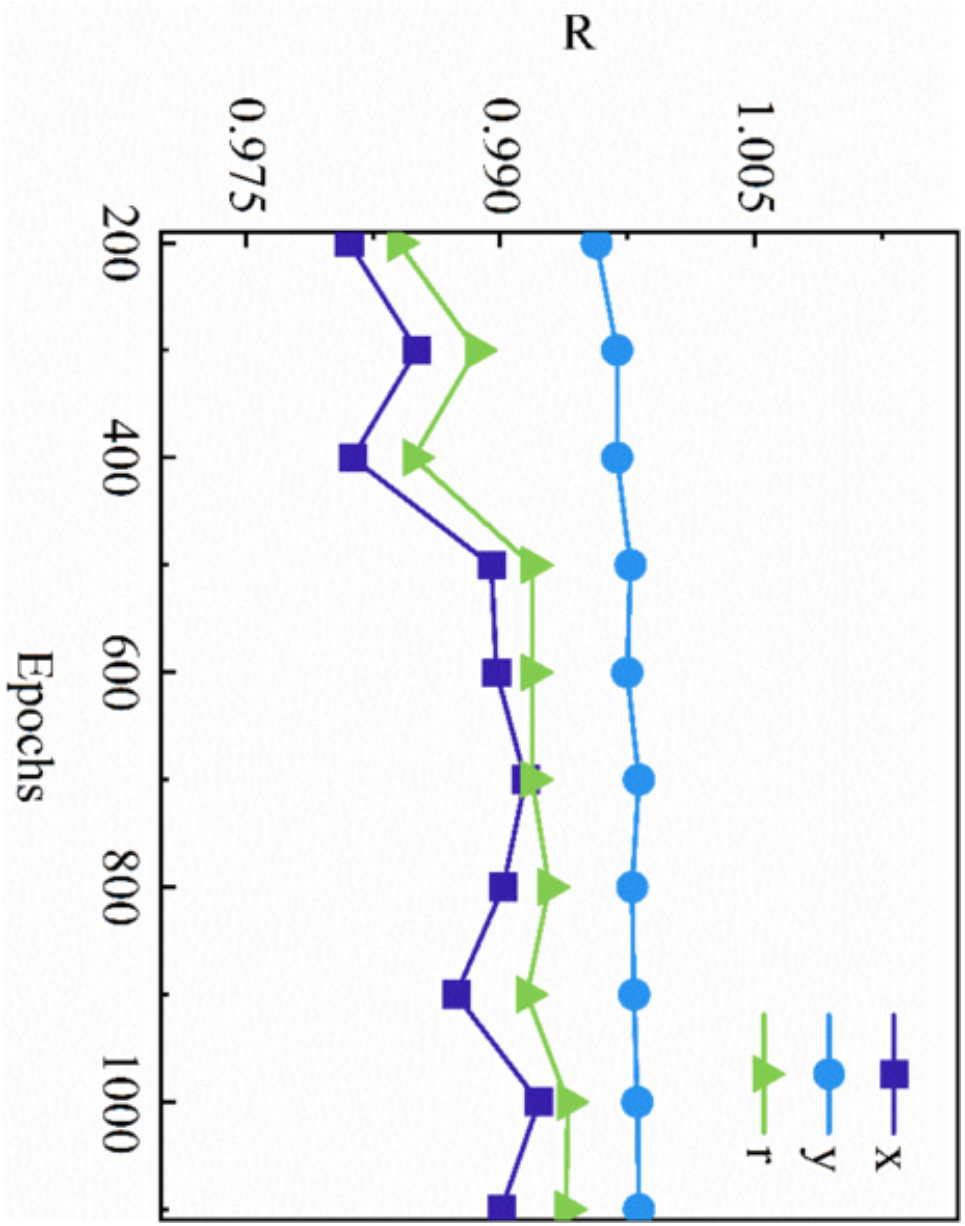

PLEASE CITE THIS ARTICLE AS DOI: 10.1063/5.0123365

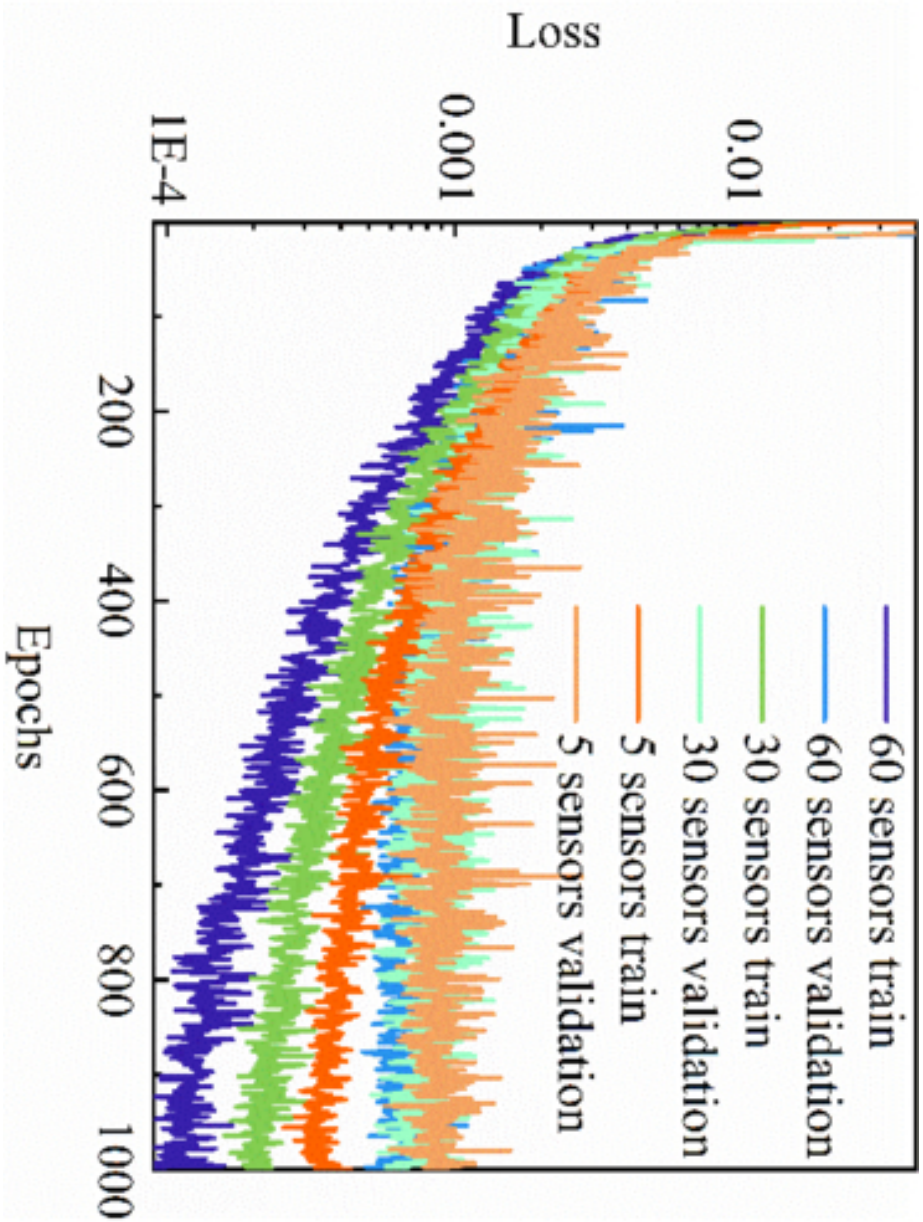

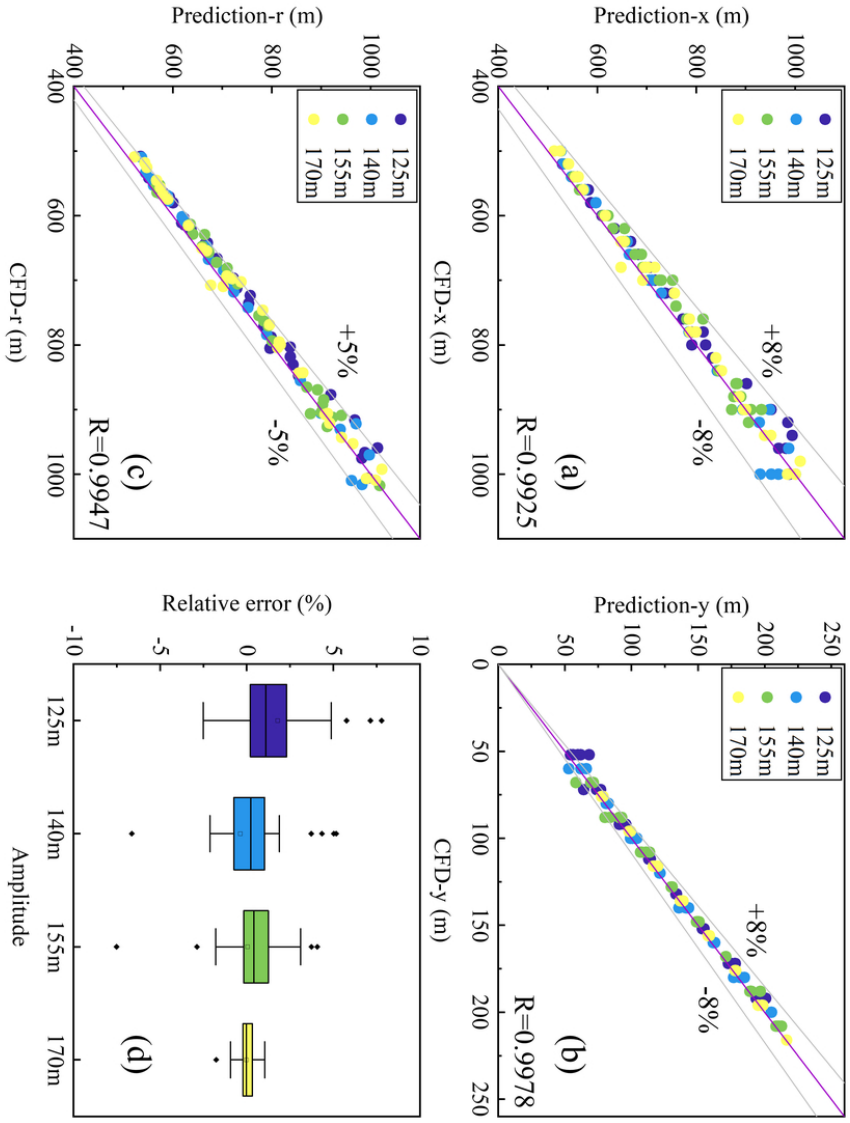

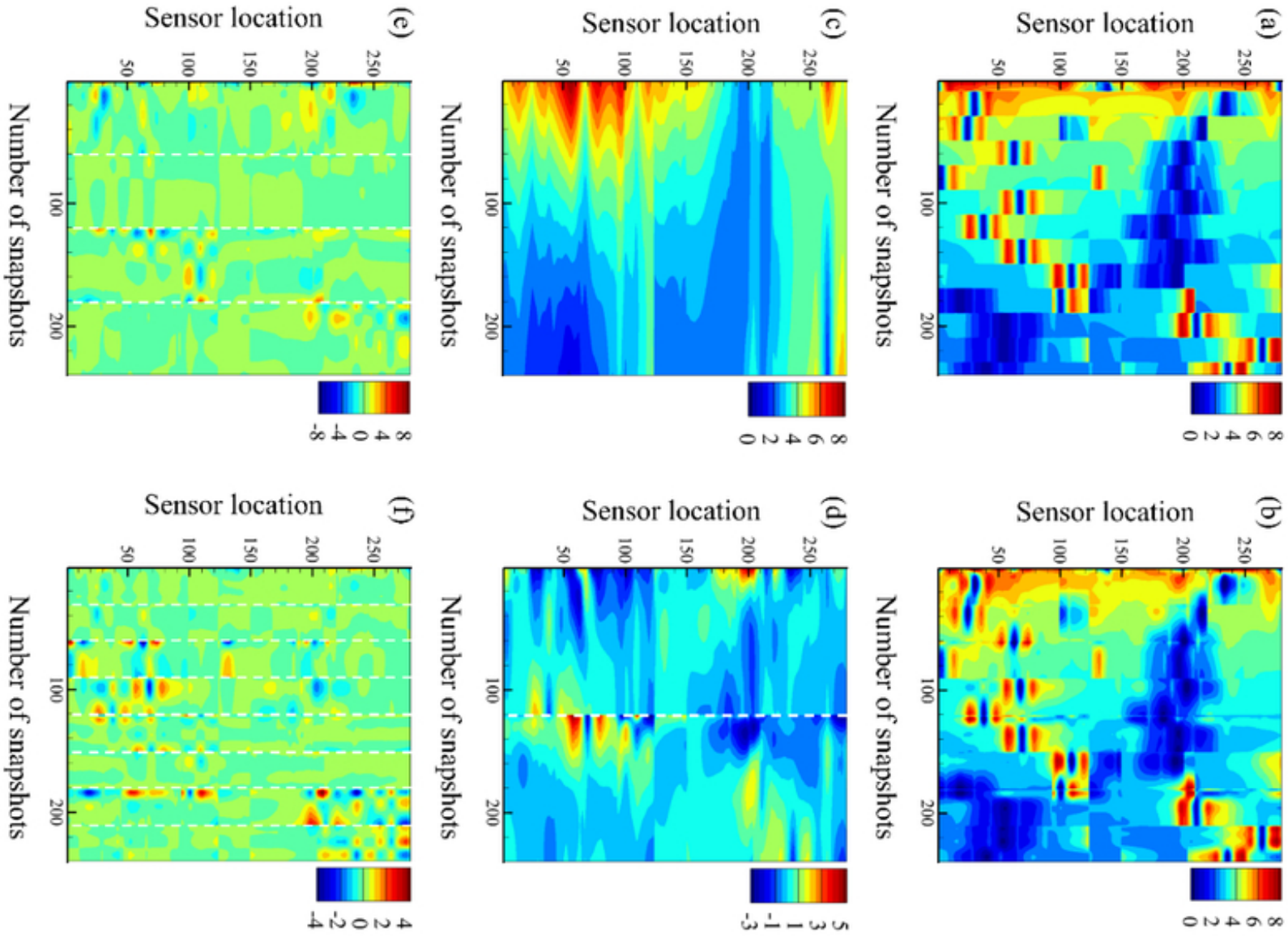

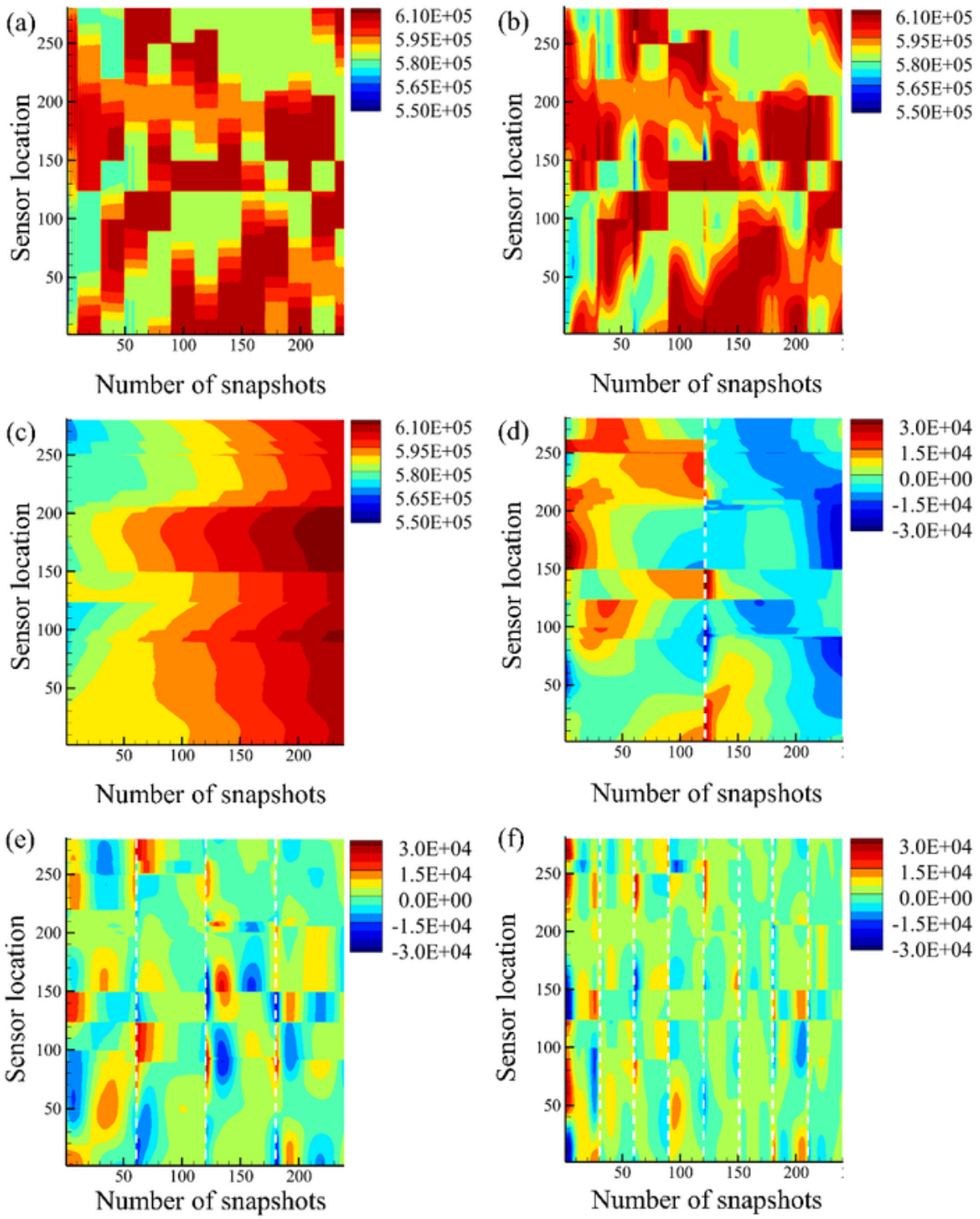

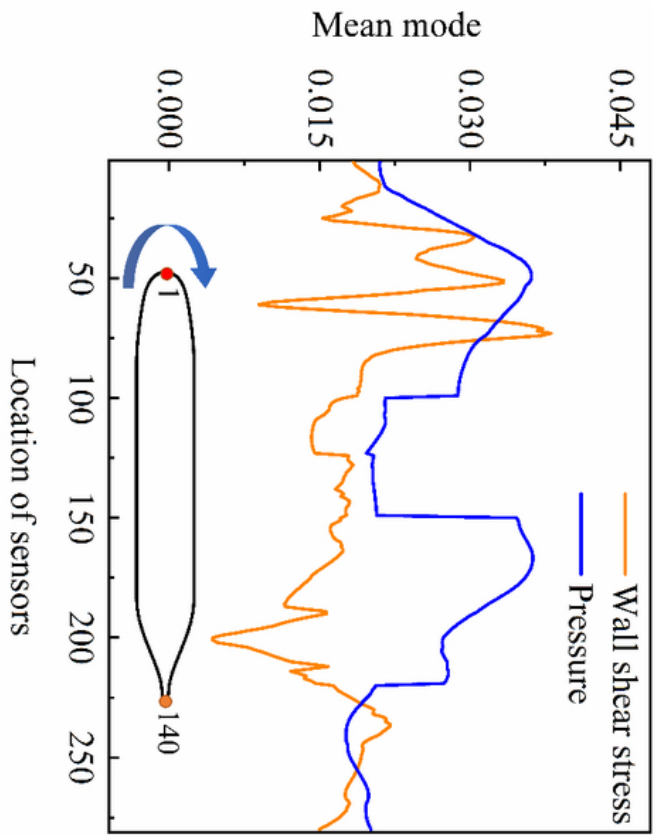

PLEASE CITE THIS ARTICLE AS DOI: 10.1063/5.0123365

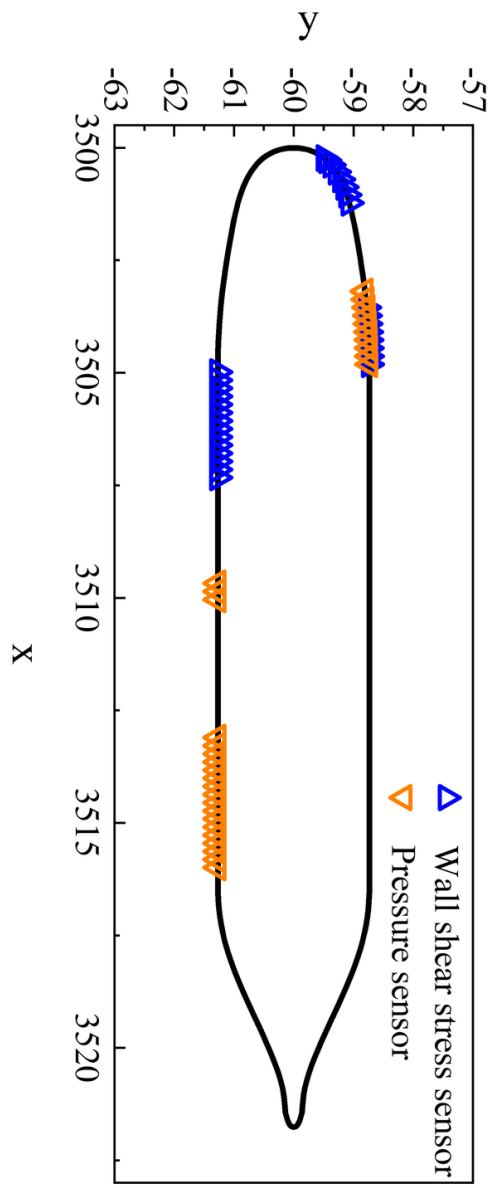

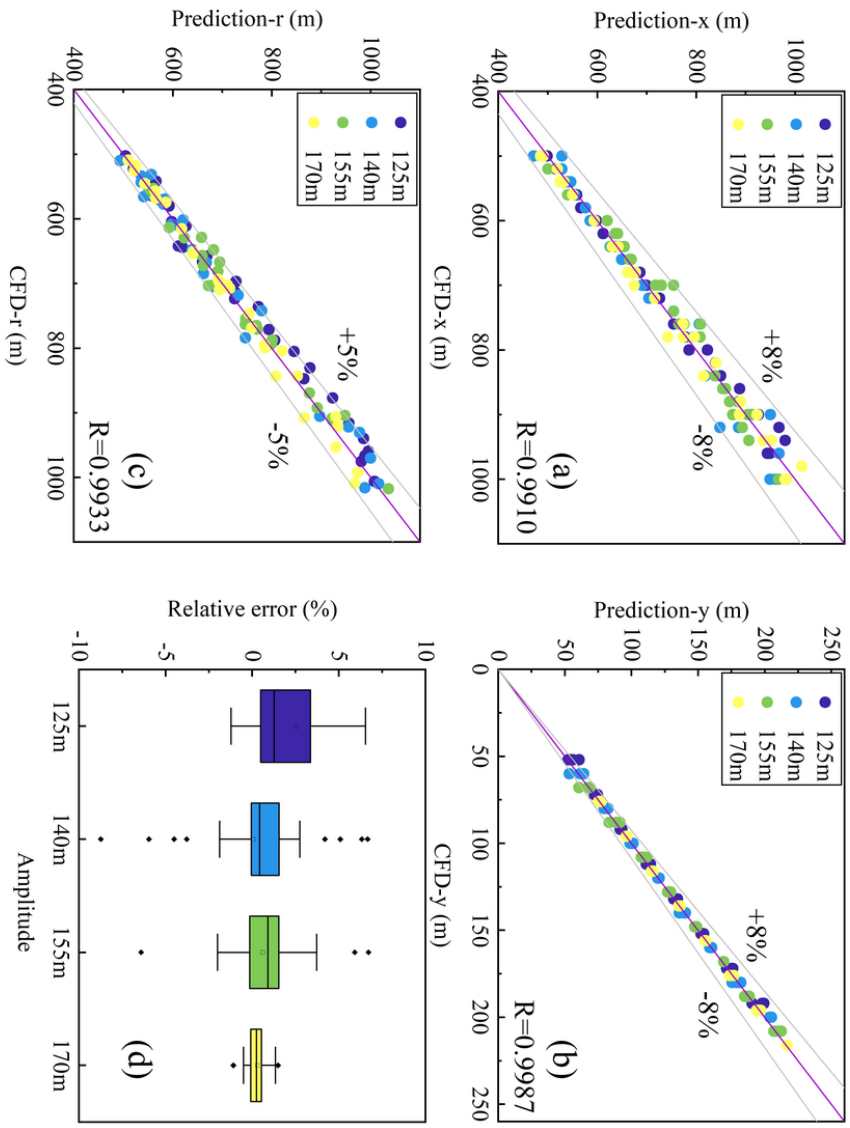

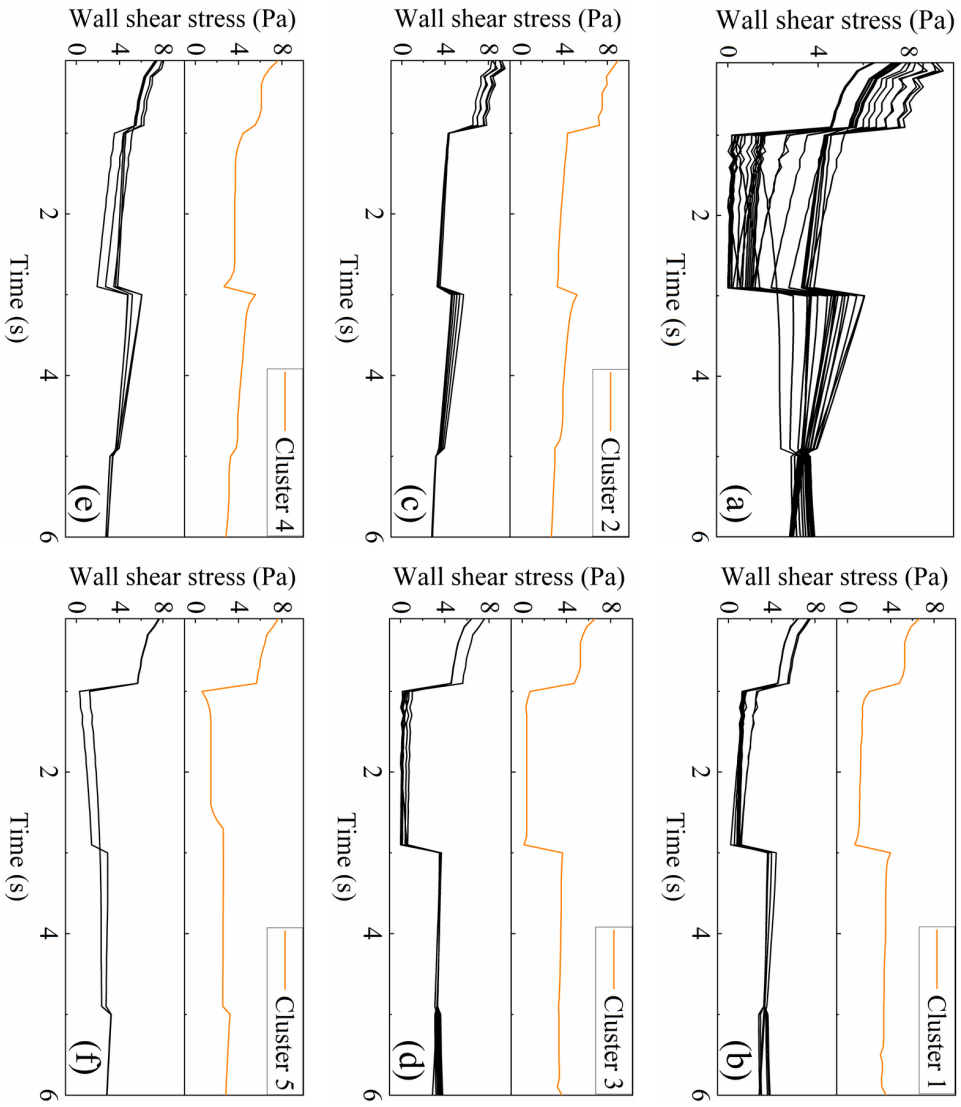

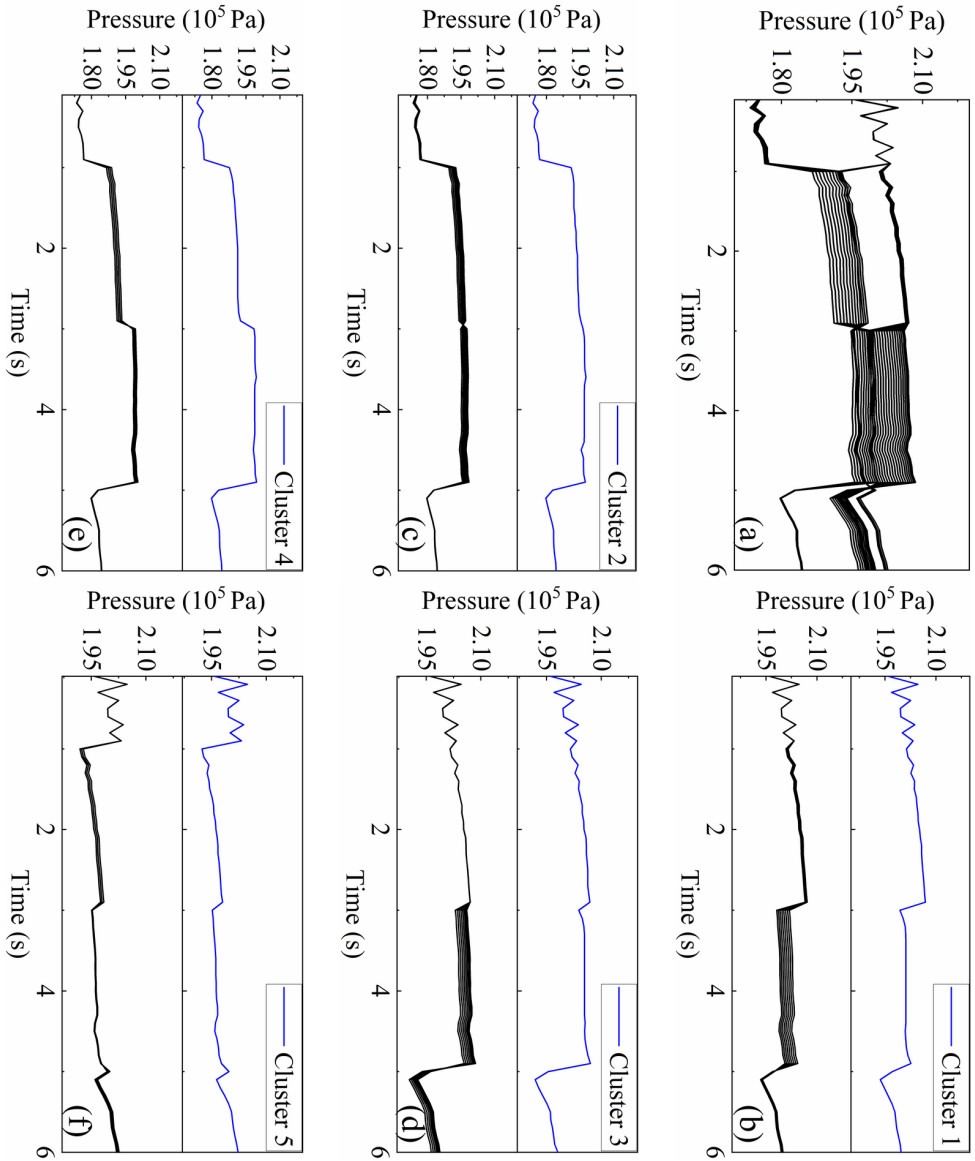

PLEASE CITE THIS ARTICLE AS DOI: 10.1063/5.0123365

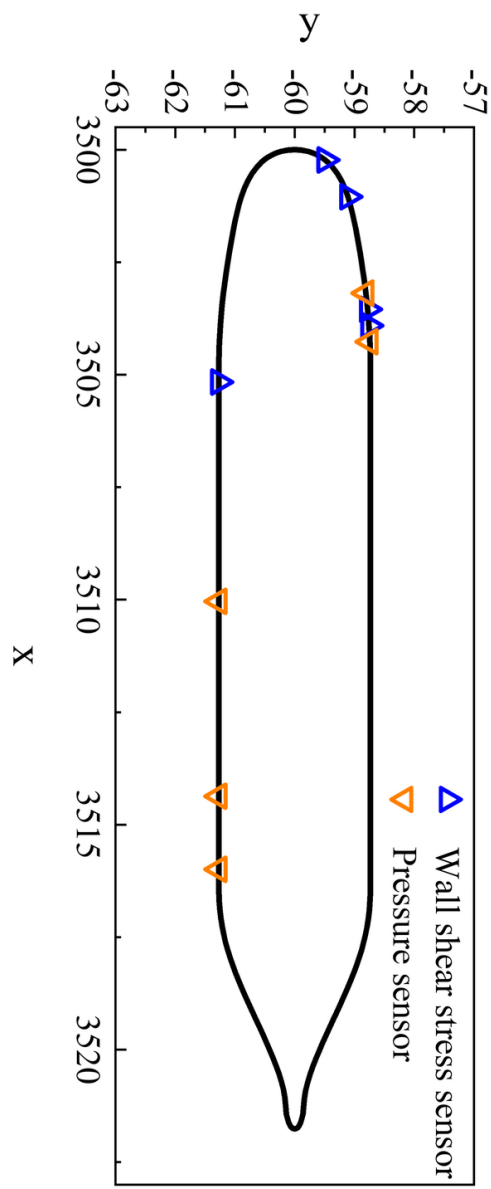

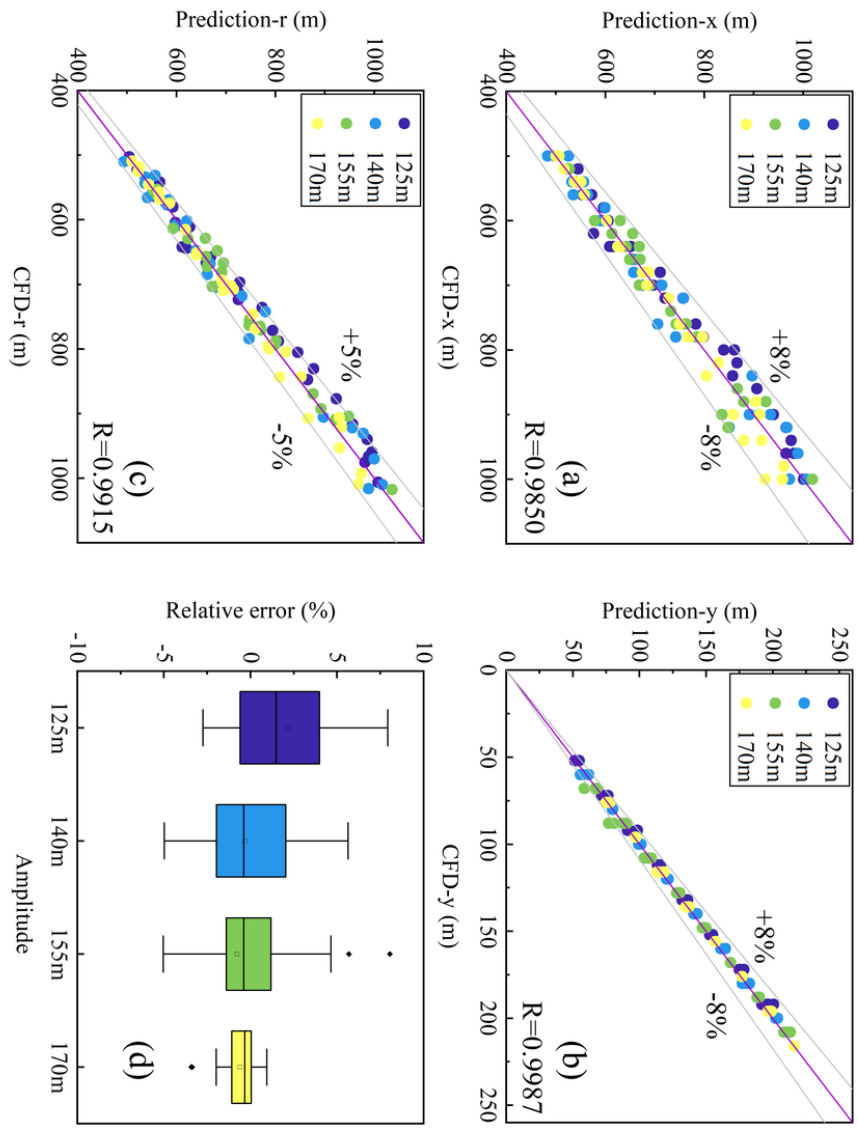

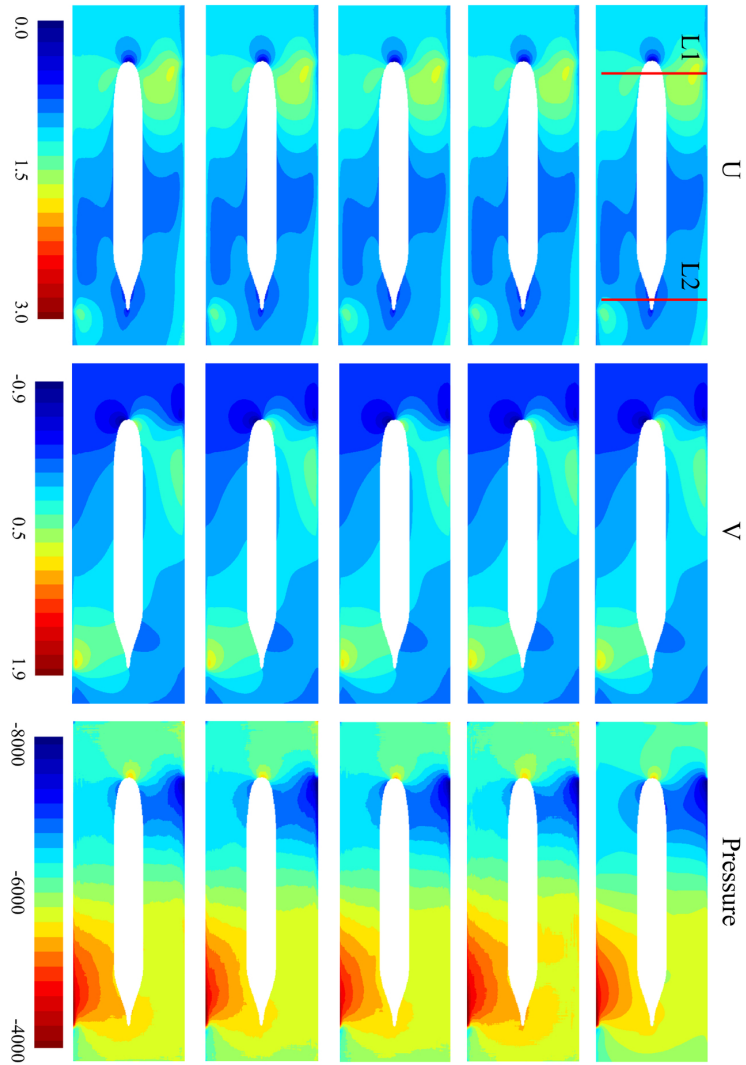

PLEASE CITE THIS ARTICLE AS DOI: 10.1063/5.0123365

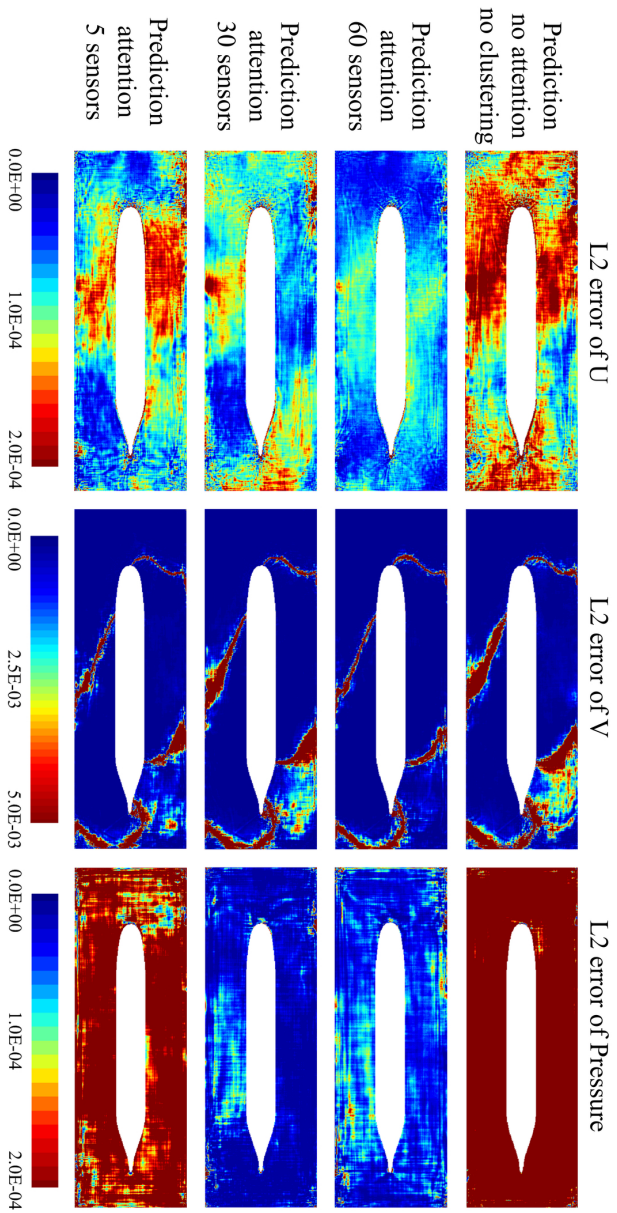

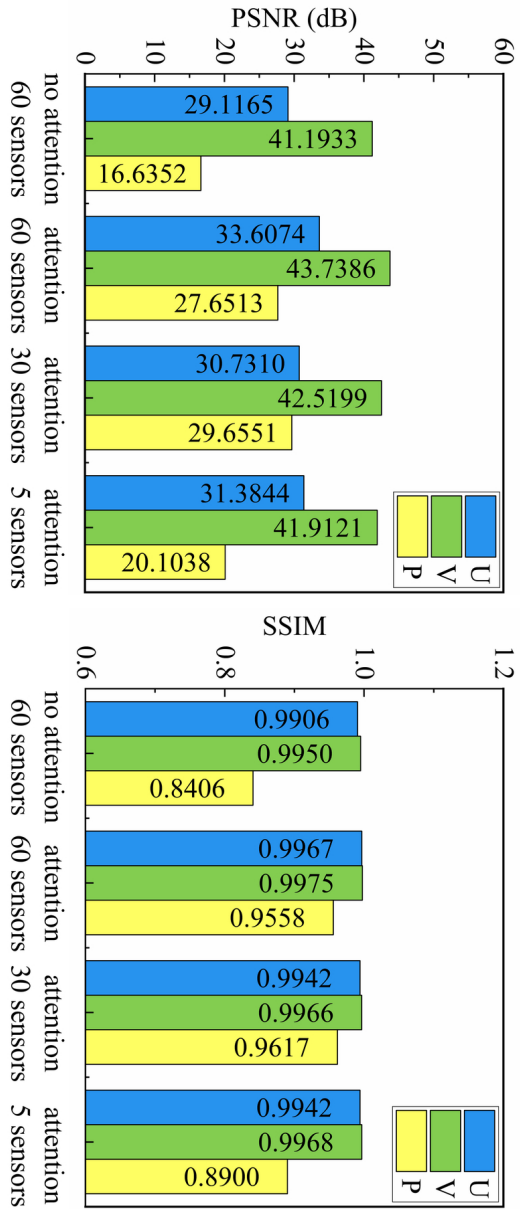

L1

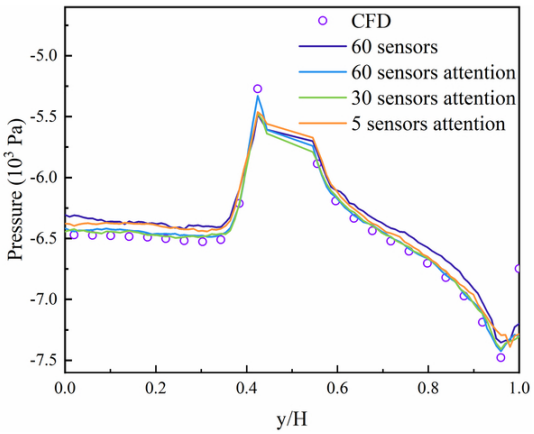

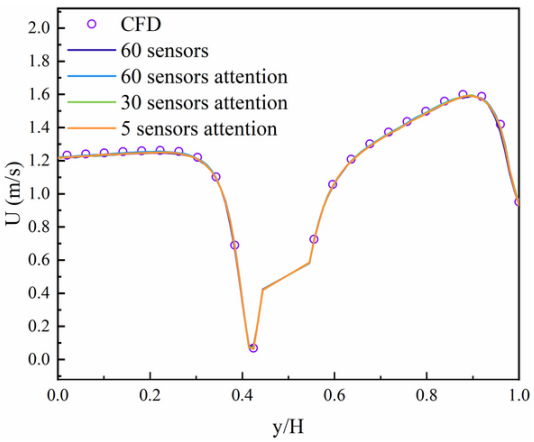

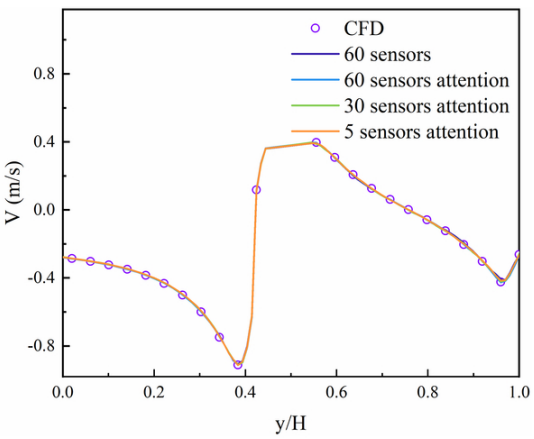

L2